iScience

CellPress
OPEN ACCESS

Article

Neuronal population models reveal specific linear conductance controllers sufficient to rescue preclinical disease phenotypes

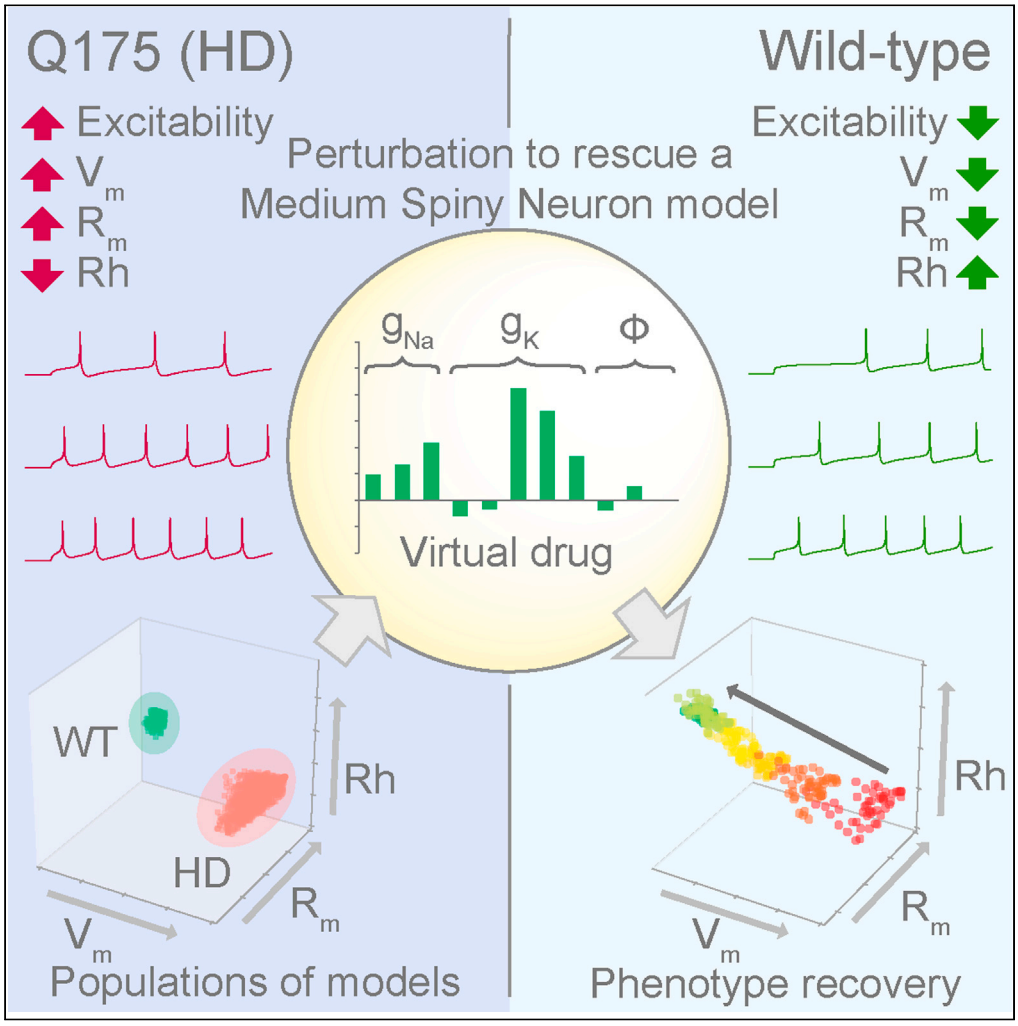

Sushmita L. Allam, Timothy H. Rumbell, Tuan Hoang-Trong, Jaimit Parikh, James R. Kozloski

kozloski@us.ibm.com

Highlights

Neuron population modeling of healthy and HD electrophysiological phenotypes

Model reconciled reduced K^+ channel expression can drive HD neuronal excitability

Reverse phenotypic screen for 'ideal' perturbations to rescue HD model's excitability

Holistic virtual drugs derived from heuristics improve upon single target modulators

Allam et al., iScience 24, 103279
November 19, 2021
https://doi.org/10.1016/j.isci.2021.103279

iScience

CellPress
OPEN ACCESS

Article

Neuronal population models reveal specific linear conductance controllers sufficient to rescue preclinical disease phenotypes

Sushmita L. Allam,[1,2] Timothy H. Rumbell,[1,2] Tuan Hoang-Trong,[1] Jaimit Parikh,[1] and James R. Kozloski[1,3,*]

SUMMARY

Preclinical drug candidates are screened for their ability to ameliorate *in vitro* neuronal electrophysiology, and go/no-go decisions progress drugs to clinical trials based on population means across cells and animals. However, these measures do not mitigate clinical endpoint risk. Population-based modeling captures variability across multiple electrophysiological measures from healthy, disease, and drug phenotypes. We pursued optimizing therapeutic targets by identifying coherent sets of ion channel target modulations for recovering heterogeneous wild-type (WT) population excitability profiles from a heterogeneous Huntington's disease (HD) population. Our approach combines mechanistic simulations with population modeling of striatal neurons using evolutionary optimization algorithms to design 'virtual drugs'. We introduce efficacy metrics to score populations and rank virtual drug candidates. We found virtual drugs using heuristic approaches that performed better than single target modulators and standard classification methods. We compare a real drug to virtual candidates and demonstrate a novel *in silico* triaging method.

INTRODUCTION

The high attrition rate of central nervous system (CNS) drugs is often attributed to off-target activity of lead candidates on neuronal ion channels leading to safety and efficacy concerns. Patch-clamp electrophysiology provides a direct way to measure biophysical properties of ion channel activity and effect on neuronal function. Pharmaceutical companies apply electrophysiology to characterize new leads' effects on neuronal ion channel activity and neuronal and network function, and *in vitro* electrophysiological assays are being implemented for pharmaceutical safety and efficacy profiling (Dunlop et al., 2008; Bowes et al., 2012; Obergrussberger et al., 2015). Electrophysiological assays for screening new cardiac drugs against myocyte ion channel activities and features are routinely performed because altered cardiac rhythms are readily observed, predictable, and life-threatening (Möller and Witchel, 2011). It is paramount in CNS drug development to similarly advance preclinical testing strategies of new chemical entities to prevent adverse drug reactions and address efficacy (Accardi et al., 2016).

It is widely acknowledged that successfully estimating the beneficial or harmful outcomes of treatments in clinical trials is complex and that failures are often attributed to estimating the average effects of the treatment across the population means while not accounting for population heterogeneity (Kravitz et al., 2004). In the CNS, the need exists to design effective drugs for individual tissues, within which physiological variability at the cellular level is pervasive (Gouwens et al., 2020; Scala et al., 2020). This need has been addressed previously through statistical tests of differences among healthy, diseased, and drugged phenotypes of neuronal populations pooled across individual neurons and across different animals (Beaumont et al., 2016). Given that a single neural tissue can integrate nonlinearly the dysfunction of a relatively small neuronal cohort (11) the urgency to optimize a drugs' total efficacy for a tissue population is acute. To that end, we employ rigorous theoretical frameworks and mathematical modeling techniques (Prinz et al., 2004; Marder, 2011; Sarkar et al., 2012; Britton et al., 2013; Gong and Sobie, 2018) and describe here a computational pipeline for discovering ionic conductance changes at the single neuron level, which together increase efficacy penetrance among target responses of a diverse neuronal population to virtual drugs. Our approach represents a method for pharmacological design that simultaneously addresses the heterogeneity of neuronal responses within a tissue while offering a path toward personalizing neurotherapeutics.

[1]IBM T.J. Watson Research Center, 13-158B, P.O. Box 218, 1101 Kitchawan Road, Yorktown Heights, NY 10598, USA

[2]These authors contributed equally

[3]Lead contact

*Correspondence: kozloski@us.ibm.com

https://doi.org/10.1016/j.isci.2021.103279

Huntington's disease (HD) is an autosomal dominant genetic disorder caused by an expanded trinucleotide CAG repeat in exon-1 of the huntingtin gene. Phenotypic changes at the single neuron electrophysiological level within the striatum, a deep forebrain structure within the basal ganglia responsible for motor, cognitive, and neuropsychiatric co-ordination, are believed to underlie symptomatic changes in motor function, cognition, and affect during HD manifestation (Ross et al., 2014). Identifying a single therapeutic mode of recovery for a dysfunctional neural tissue also undergoing neurodegeneration, such as striatum in HD, is challenging owing to the biophysical diversity of the single neurons comprising the tissue, their adaptive drivers, electrophysiological set points (O'Leary et al., 2014) and the confounding effects cell loss can have on normal circuit function (Zheng and Kozloski, 2017). Commonly referred to as medium spiny neurons (MSNs), the principal neurons of the striatum exhibit varied active and passive properties in healthy and diseased phenotypes and manifest electrophysiological disease phenotypes (André et al., 2011). MSNs are also the neuronal population most vulnerable to insult in Huntington's disease. Here we present an example of striatal neuron model populations for Huntington's disease (HD) and for their wild-type (WT) background population (André et al., 2011).

Prior experimental studies have explored alterations to physiological and morphological measures among MSNs. Altered active and passive membrane properties such as resting membrane potential, rheobase, input resistance, and firing rate were quantified among MSNs expressing D_1 dopamine receptors (D1-type) or D_2 dopamine receptors (D2-type), and across different HD animal models and healthy and HD phenotypes (Klapstein et al., 2001; Planert et al., 2013; Goodliffe et al., 2018). MSNs have been central to studies of pharmacotherapies, such as inhibition of phosphodiesterases (PDEs) of the CAMP and CGMP pathways, aimed at alleviating the above membrane properties both *in vivo* and *in vitro* (West and Grace, 2004; Beaumont et al., 2016). How these pathways engage ion channel proteins via DARPP-32 substrate modulation (Greengard et al., 1999) and regulate the membrane activity in WT and HD phenotypes has yet to be fully understood. Prior *in vitro* and immunofluorescence studies in HD transgenic mouse models detected decreased K+ channel proteins (Kir2.1, Kir2.3, Kv2.1) in MSNs (Ariano et al., 2005). However, it remains unclear if these membrane protein changes are sufficient to explain the altered electrophysiological properties and subsequent vulnerability of MSNs in HD.

Here we present a generic modeling framework that enables building populations of models (PoMs) with characteristics of healthy and diseased neuronal phenotypic categories. We demonstrate parallel approaches to combine statistical and machine learning methods and uniquely identify virtual drugs, which target ion channels and rescue the disease population phenotype toward a healthy phenotype. We also show how scoring these virtual drugs based on their ability to rescue the disease phenotype may be performed based on both heterogeneity and divergence of the neuronal PoMs comprising the phenotype.

Current model-based regulatory evaluations have mainly centered around PK/PD simulations, but with growing impetus for inclusion of *in vitro* electrophysiological assays for safety and efficacy screening of CNS drugs (Accardi et al., 2016), our methods complement triaging strategies to optimize therapeutic target design, which remains an area of strong interest among the pharmaceutical industry.

RESULTS

Thus far, there have been few drugs approved for treatment of HD, with most treating chorea and movement disorders (Coppen and Roos, 2017). Some antiepileptic drugs are prescribed for various neurological disorders (including HD) and target neuronal excitability through modulation of ion channels. The main mechanisms of action of these drugs, in addition to targeting voltage-gated ion channels, are modulation of glutamatergic and GABAergic neurotransmission and intracellular signaling pathways (Rogawski and Löscher, 2004). Due to the preclinical success of a PDE10 inhibitor (i.e., the PDE10i known as PF-230920) in rescuing *in vivo* and *in vitro* neurological deficits in HD symptomatic animal models, the path to clinical trial was taken for this PDE10i, but the drug failed to ameliorate motor and functional disturbances in HD patients (Beaumont et al., 2016; Rodrigues and Wild, 2017). Therefore, the failure of the Pfizer Amaryllis trial made clear that finding a drug candidate based on current preclinical criteria triaging methods does not necessarily predict the successful outcome of subsequent human clinical trials. There exists not only a need for better drug design, but also for a better means of preclinical scoring and deciding which drugs should enter clinical trial, such that designing drugs and clinical trials that maximize translatability and ability to mitigate clinical endpoint risk of failure might become possible (Wehling, 2009).

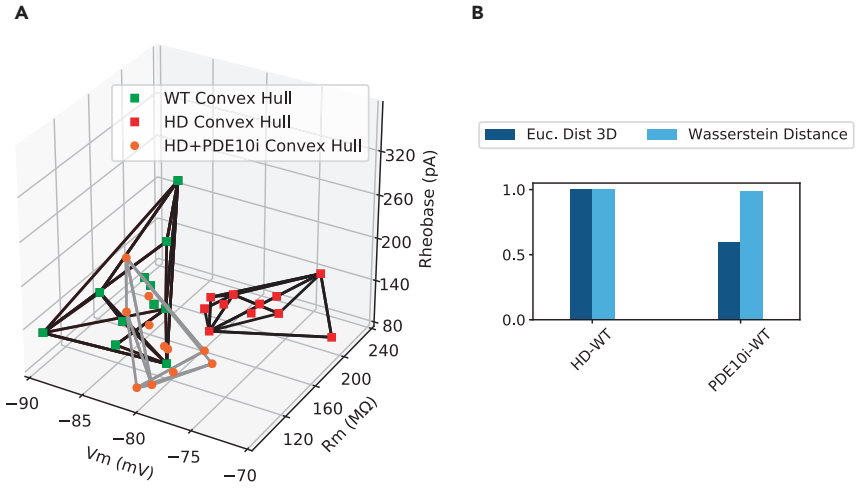

Figure 1. Efficacy evaluation metrics

(A) Convex hulls enclosing WT, HD and PDE10i treated HD phenotypes in three dimensions representing membrane properties of MSNs illustrate the location of each phenotype in feature space.

(B) Distance metrics used to score the performance of the PDE10i drug for its ability to recover the HD phenotype in feature space (right bars), quantified as a proportion of the original Euclidean distance and Wasserstein distance between WT and HD PoMs (left bars; normalized to 1.0).

Metrics for scoring efficacy of phenotypic recovery

We used the pre-clinical *in vitro* data from Beaumont et al. (2016), precursors to Pfizer's Amaryllis trial, in order to quantify using our multivariate methods how well the drug recovered compromised neuronal excitability in the Q175 disease phenotype model. To assess the extent of separation in the space of the measured neuronal phenotypes (single neuron excitability features) we used convex hulls, which provide the smallest convex set of enclosure of points for a dataset (Eddy, 1977). In Figure 1A, we show convex hulls that visualize the enclosures of data from the WT (green) and HD (red) phenotypes in a three-dimensional (3D) feature space, comprising passive membrane properties of MSNs. The phenotype of MSNs rescued by the pharmacotherapy of the PDE10i is represented by the convex hull of HD+PDE10i (orange), which intersects the WT convex hull space. We quantified the performance of the drug by extracting two 3D metrics from the data for the distance between both HD and HD+PDE10i phenotypes and the WT phenotype, Euclidean distance (ED3) and Wasserstein distance (see STAR Methods), and we report values normalized to the HD-WT distances for comparison. The resulting HD-WT distances were normalized to 1.0, and for the drug treated phenotype HD+PDE10i, ED3 was 0.6 and Wasserstein distance was 0.98 (Figure 1B). While an ED3 reduction of ~40% indicates that the HD+PDE10i population mean is closer to the WT mean than the HD mean was, the lack of reduction in the Wasserstein distance metric despite the closer means indicates that the covariance among features must be further from the WT feature covariance in the HD+PDE10i case than the HD case. We conclude that based on these preclinical data, PDE10i was advanced as a viable HD drug candidate based on a recovery of ~40% of the Euclidean distance metric but a mere ~2% improvement in Wasserstein distance metric of divergence between the distributions.

Population of models for characterizing WT and HD electrophysiological phenotypes

We wondered if a computational model of the MSN (Mahon et al., 2000; Octeau et al., 2019) might allow further refinement of our characterization of the preclinical data from Beaumont et al. (2016). Creation of large databases of model neurons can provide insight into how neuronal membrane response properties are determined by the underlying ionic conductances (Prinz et al., 2004) and help elucidate neuronal population and intersubject variability (Britton et al., 2013). We created a database of WT and HD phenotypes from different instances of the model, thus creating two PoMs. These PoMs reproduced the empirical ranges of membrane properties (Figure 2). In Figure 2A, green and red squares represent the original preclinical data from 11 neurons for WT and HD respectively. To create the PoMs, an evolutionary algorithm described in Rumbell and Kozloski (2019) was used (see STAR Methods) to explore the model's eleven dimensional parameter space, with each dimension representing one of eight active ionic conductances and three specific ion permeability parameters (see Table 1 for details of parameter ranges used for

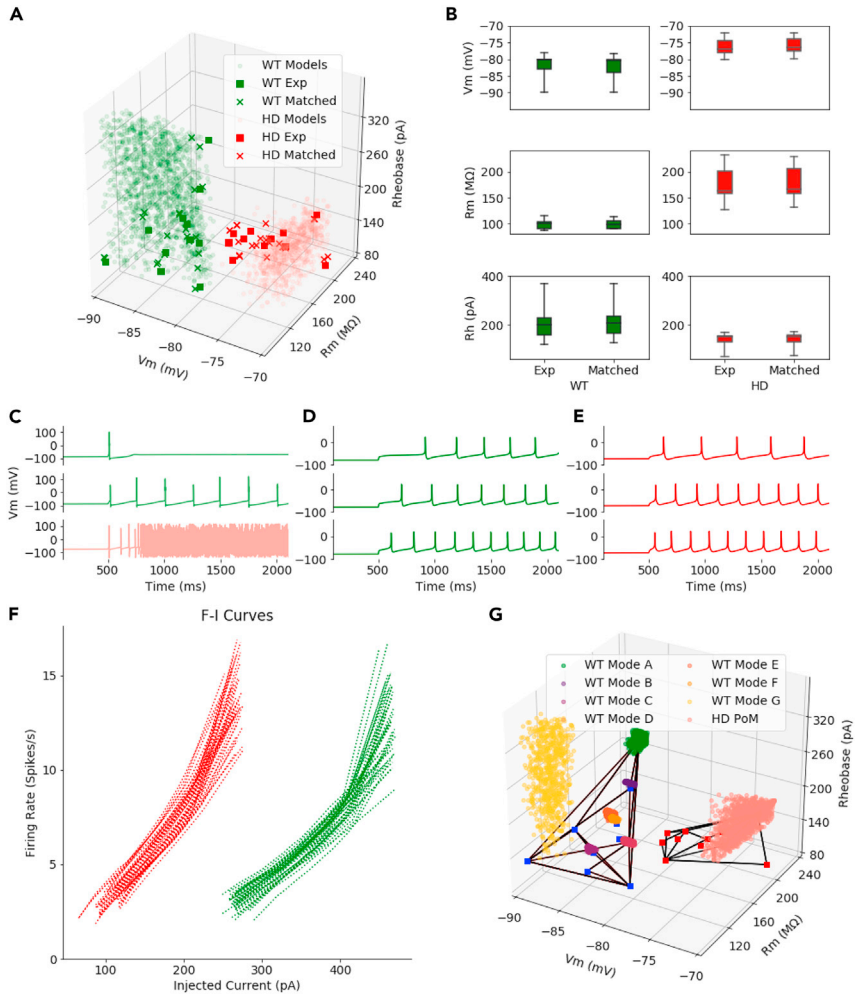

Figure 2. Population of models to characterize WT and HD phenotypes

(A) Evolutionary algorithm generated PoMs for WT and HD phenotypes. Light circles show PoMs, solid squares show experimental data, and the subset of each PoM matched to the empirical data using k-nearest neighbors search are shown as 'x'.

(B) Box plots of the three membrane properties of the matched models and empirical data are similar (two sample K-S test statistic for WT V_m($p = 0.63$), R_m ($p = 0.63$), and rheobase ($p = 0.96$); HD: V_m ($p = 0.82$); R_m ($p = 0.96$); Rheobase ($p = 0.83$)).

(C) 50% of matched models exhibit unrealistic spiking behavior. Top and middle example models from the WT PoM shown in green. Bottom example model from the HD PoM shown in red.

(D and E) Addition of further spiking feature constraints to ensure the PoMs exhibit realistic spiking patterns of WT (D) and HD (E) phenotypes

(F) F-I curves of WT (green) and HD (red) PoMs show heterogeneity within each PoM, and lowered excitability in HD.

(G) Additional spiking constraints collapsed the feature space for the PoM of the WT phenotype into islands of feature space when additional optimizations were performed. Multiple islands (modes) of feature space were uncovered through both multiple random seeds, and optimizations targeting specific empirical data points.

sampling). Separate optimization runs targeting each phenotype, WT and HD, generated PoMs with output features bounded by specified ranges. The WT PoM comprised 1650 different parameter settings (Figure 2A, light green circles), while the HD PoM comprised 859 (Figure 2A, light red circles). Model instances within the WT and HD categories spanned the range of all three membrane features (Figure 2A). These three membrane features were specifically chosen because each was available from empirical data from Beaumont et al. (2016) and together they were used as evidence from preclinical *in vitro* studies to determine the effectiveness of the PDE10i drug in alleviating these features of the HD phenotype. From this large database of models, we sampled models to generate a joint distribution across all three feature dimensions, comparable to that of the empirical data, using the *k*-nearest neighbor algorithm (see STAR

Table 1. Parameter ranges explored by the evolutionary optimization algorithm.

Conductance parameters	Units	Lower bound	Upper bound
KDR	pS/μm^2	0.6×10^{-4}	6.0
KIR	pS/μm^2	1.5×10^{-6}	0.15
KAf	pS/μm^2	9×10^{-7}	9×10^{-2}
KAs	pS/μm^2	3.2×10^{-7}	0.32
KRP	pS/μm^2	4.2×10^{-7}	0.42
Nat	pS/μm^2	35×10^{-4}	35
NaP	pS/μm^2	2×10^{-6}	2×10^{-2}
NaS	pS/μm^2	1.1×10^{-6}	0.11
Permeability parameters			
P_{CLC}	μm/ms	1e−10	1×10^{-6}
P_{NALCN}	μm/ms	1e−10	1×10^{-6}
P_{KCNK}	μm/ms	1×10^{-9}	1×10^{-4}

Methods). The sampled models, comprising the two nearest models for each empirical observation, are each indicated by '×' among the cloud of all model instances. Box and whisker plots summarize the experimental data from (Beaumont et al., 2016), and the sampled models for both WT and HD phenotypes (Figure 2B) show good agreement between model outputs and the data (two sample K-S tests for WT V_m: p = 0.63, R_m: p = 0.63, and rheobase: p = 0.96; HD V_m: p = 0.82, R_m: p = 0.96, and rheobase: p = 0.83). We could, therefore, sample model instance feature values from the same distribution as the experimental data. The evolutionary search and subsequent sampling methods allowed us to create PoMs in close proximity to the preclinical data in feature space. This PoM generation framework is robust for creating PoMs representative of different empirically observed phenotypes by varying the parameters of a single underlying mechanistic model.

To examine the spiking properties of the sampled models, we then applied several step current injection protocols. Our first optimization only targeted three membrane properties (V_m, R_m, Rh), and therefore no specific features of MSN spiking activity, such as AP height, after-hyperpolarization potential (AHP), coefficient of variation of interspike intervals (ISI CV), time to first spike (TFS; also termed 'spike latency') and firing rate (FR), were optimized. Without constraints on active membrane properties, in some cases our optimized and sampled models failed to reproduce spiking features characteristic of MSNs. We observed that ~50% of these models entered depolarization block under physiological step current injection. Because the empirical data reported in Beaumont et al. (2016) did not include raw traces from which to extract these spiking features, we decided to make the assumption that the empirically sampled neurons did not enter depolarization block and proceeded to survey the literature to obtain normal measurements for each spiking feature (Klapstein et al., 2001; Planert et al., 2013), thus establishing their acceptable ranges for our subsequent refining of the MSN PoMs (See STAR Methods, Table 2).

New optimization runs targeted the 11 features reported in Table 2. The first seven features of this table, RMP, Rm, Rheobase, AP height, AHP, spike latency and firing rate at Rh+50pA, are crucial to define the adherence of model behavior to realistic spiking characteristics of MSNs and were used to calculate the distance metrics later in this study. This optimization found 1219 WT and 1223 HD models constrained by the complete set of 11 feature ranges and 3 additional features such as firing rate at Rh+100pA within different time windows. Models had regular firing patterns, and none entered depolarization block when injected with current stimuli ranges up to rheobase plus 100 pA (Rh+100pA; Figures 2D and 2E). Model outputs each showed characteristic spike latencies that were greater in WT models than in HD models, and each showed higher firing rates with increasing depolarizing stimulation across both phenotypes as observed in (Klapstein et al., 2001; Planert et al., 2013). Figure 2F shows F-I curves obtained from 20 models for each phenotype, constructed using step currents in increments of 20pA from Rh-60 pA to Rh+100 pA. The HD models had a lower rheobase and exhibited hyperexcitability (red in Figure 2E), whereas the WT models had a higher rheobase (green in Figure 2E). Heterogeneity of F-I curves are seen across both populations.

Table 2. WT and HD feature ranges targeted by the evolutionary optimization algorithm.

	WT		HD	
Feature name	Target mean	Target deviation	Target mean	Target deviation
Features included in optimization and included in metric distance calculations				
Resting membrane potential RMP (mV)	−84.0	6.0	−76	4
Rheobase Rh (pA)	245	126	123	53
Membrane resistance Rm (MΩ)	102.5	12.5	180	50
Firing rate at rheobase +50pA FR50 (Spikes/s)	6	4	6	4
AP height (mV)	27	10	27	10
AHP (mV)	−50	10	−50	10
Time to first spike TFS50 (ms)	400	300	400	360
Feature included in optimization but excluded from metric distance calculations				
Time to first spike TFS100 (ms)	400	350	400	380
Firing rate at rheobase +100pA FR100 (Spikes/s)	12	8	12	10
Coefficient of variation of Inter spike interval ISI_CV*	0	1	0	1
Voltage base variance (mV)	0	0.1	0	0.1

The evolutionary algorithm produced PoMs that conformed simultaneously to the three membrane feature ranges of WT and HD empirical observations, as well as generic descriptions of MSN active spiking properties (Figure 2F). However, these new PoMs failed to capture the full range of empirical diversity among the three properties (V_m, R_m, Rh) to the same extent that the original PoM from our less constrained optimization did (Figure 2A). The new HD PoM (1223 models) was reasonably well spread within the convex hull of HD empirical data (black boundary in Figure 2F) but, again, not as well as the original HD PoM, and the new WT PoM (1219 models) was clustered at one vertex of the convex hull of WT empirical data and thus did not sample the entire WT convex hull. This clustering is a commonly observed phenomenon when generating populations of biophysical models by evolutionary algorithms, as increasing the number of objectives tends to decrease the variability in observed feature values (Gouwens et al., 2018). To check for the ability of the model to access alternate feature values within the model parameter space, we performed several additional evolutionary optimization runs. We performed the optimization with 5 different random seeds, which resulted in identification of a second feature mode of WT models, again matching our target features but occupying a different region of feature space (Mode G in Figure 2G). The two modes of WT feature space identified by population-based optimization encompassed 2 out of 11 WT data points from the Beaumont et al. (2016) data. To facilitate coverage of additional empirical population modes, we performed 5 additional optimizations targeting specific empirical data points more precisely, each matching the target feature values for Rm, Vm, and rheobase to those of a specific empirical data point, and reducing the feature range for those three features to within 10% of the values specified in Table 2 (see supplemental information for more details). After simulating a total of approximately 1,530,000 models, these additional optimizations were unable to find parameter sets resulting in feature values matching all criteria simultaneously (i.e., error value of 0), so for each optimization run we relaxed these additional constraints and allowed for models with non-zero error values. To identify the most appropriate WT model population for proceeding with our analysis, we down-sampled models to ~30,000 that are within zero error ranges or within close proximity of feature ranges specified above. We calculated the Wasserstein distances in 3 dimensions between the HD population and each WT population and compared these distances with the empirical Wasserstein distance between HD and WT neurons. The WT population from the first optimization run gave the largest Wasserstein distance from the HD phenotype among all trials (Figure S4), so we selected that population for subsequent analyses as the most challenging required target

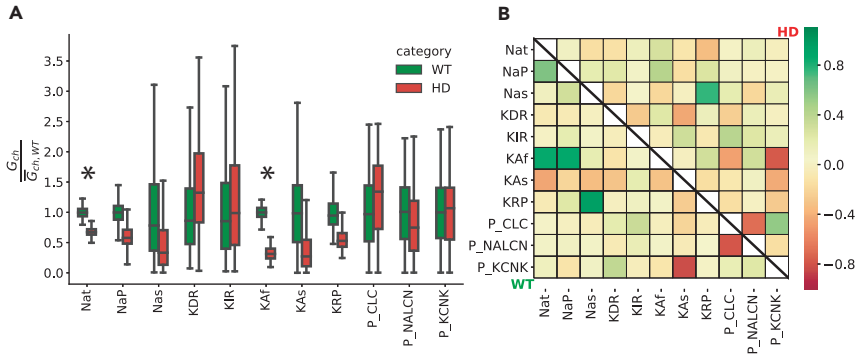

Figure 3. Analysis of parameters of the WT and HD PoMs reveals decreased ionic conductance changes associated with HD pathology

(A) Box plots of ionic conductance parameter values comprising the WT (green) and HD (red) phenotype PoMs. Values are normalized to the mean parameter values for the WT model. Ionic conductance densities that show significant differences between WT and HD (K-S distance >0.9) are indicated with "*".

(B) Correlation matrix of the ionic conductances within the WT PoM (lower triangle) and the HD PoM (upper triangle). Diagonal is left blank. Correlations between some conductances (e.g., the subthreshold slow sodium, Nas, and persistent potassium, KRP) are conserved across the two phenotypes.

perturbation. Note that the same analyses described below and applied to the other WT population modes would not have qualitatively changed the outcome of the study, and results from other random seeds are discussed in the supplemental information. In general, optimizations of PoMs encounter problems when adhering to many feature constraints simultaneously. Despite these limitations to sampling, we observed that both model populations (WT and HD; Figure 2F) were significantly different from each other (one-way ANOVA, $p < 0.0001$). This difference is consistent with the statistical differences among the empirical observations of Beaumont et al. (2016).

In summary, we constructed a large database of models (~2,400), that strictly obeyed the active properties of MSNs, specifically AP height, AHP, spike latency, firing rates, and ISI CVs. These models also approximated passive membrane properties that distinguished WT and HD MSNs. Furthermore, in our subsequent analyses, the more narrowly constrained WT models (Figure 2F) presented an even more challenging target than their empirical counterparts for ameliorating HD models using virtual drugs. We propose that provided the underlying model is a good one, any successful virtual drug identified under these specific, more stringent criteria for resolving HD phenotypic disturbances, should also in general demonstrate our methods and be able to recover the WT phenotype from the HD phenotype.

Analysis of parameters reveals ionic conductances associated with phenotypic differences

We further analyzed the parameter distributions underlying our PoMs and created a reverse screen for the origins of neuronal excitability differences among the HD and WT phenotypes. Box plots of ionic conductance parameter values comprising the WT (green) and HD (red) phenotype PoMs normalized to the mean of the WT models are shown in Figure 3A. The most significant difference predicted by the PoMs is a downregulation in KAf conductance, which further corroborates experimental evidence for intrinsic excitability being mediated by Kv channels (Kang et al., 2014; Carrillo-Reid et al., 2019). The transient Na conductance was also significantly downregulated in our HD models, and while to our knowledge no direct evidence of reduced expression of Nav1.2 channel proteins in HD exists, there is evidence for sodium channel β4 subunit downregulation in HD transgenic animals, which may underlie neuritic degeneration (Oyama et al., 2006). We calculated a K-S test statistic between WT and HD model parameters and found those parameters for which the K-S distance was ≥ 0.7: for Nat, 0.95; for KAf, 1.0; for NaP, 0.73; and for KRP, 0.76. We also note, however, that when considering multiple PoMs at different modes in WT feature space, alternate hypotheses emerged about which potassium and sodium channels are responsible for deficits in outward and inward conductance between WT and HD neurons (for example with KRP and Nas emerging as the largest differences in modes B and F (Figure S3)).

We also examined correlations among the parameters by constructing a heatmap representing pairwise correlations between model parameters (Figure 3B). WT model parameter correlations are shown in the

lower triangle of Figure 3B, and HD model parameter correlations shown in the upper triangle. A strong correlation between Nat and KAf exists (r > 0.8), which is diminished among HD phenotypes (r~0.3). We next assessed how the ionic conductance parameters were correlated to each of the first 7 features from Table 2. We applied linear regression methods (Sarkar and Sobie, 2010) (see Figure S5) to uncover the relationships between each of the model's ionic conductances and the features of model outputs for both phenotypes. The linear regression coefficients indicate the sensitivity of the perturbation of individual conductances and their influence on the relative model properties against which they were regressed. The firing rate property was most sensitive to two conductances: NaS and KRP (Figure S5). These two conductances were highly correlated among both WT and HD models seen in Figure 3B (a correlation also present in alternate WT modes (Figure S3)). Both of these ionic conductances have long time constants of activation, which may underlie their ability to maintain subthreshold excitability and alter repetitive firing rates (Hoehn et al., 1993; Nisenbaum et al., 1996). The coefficients that most influenced rheobase, a critical differentiating feature of the phenotypes, were P_{KCNK} (permeability to K+ ions) in both phenotypes, followed by KAf conductance. This is not surprising as prior experimental work quantified the effects of potassium leak on depolarization and rheobase of striatal neurons (Octeau et al., 2019). Overall, most of the features could be predicted well with linear models (R^2 values >0.9; see Supplementary Results) with the exception of spike latency feature for WT, where the goodness of fit measure was low (R^2 = 0.3), but a polynomial regression fit with order 2 improved the R^2 value to 0.6 (not shown).

Virtual drug design

While the methods described above that are useful to characterize parameter sensitivity with respect to model features, they are insufficient to reveal a coherent target modulation profile, i.e., a set of perturbations of ionic conductance parameters of the model sufficient to rescue excitability phenotypes in HD. We have termed these unique combinations of ionic conductance perturbations 'virtual drugs' and present the various methodologies we evaluated to efficiently recover the HD phenotypes toward the WT phenotype feature space. 'Efficient recovery' refers to perturbing the model parameters such that the resulting treated HD models' output feature distributions are in close proximity to the WT models' feature distributions within a multidimensional measurement space, calculated according to our distance metrics. We demonstrate and present the results of these methodologies in the following sections.

Single target modulation

Fast inactivating potassium conductance, KAf, was significantly downregulated in the HD PoM (Cohen's d measure >3). Accordingly, we considered gKAf to be a key parameter, as it was highly correlated to features such as TFS, Rheobase, and FR (see Supplementary Results), and was the strongest coefficient of the first principal component that explained 36% of the variance in the combined WT and HD PoM's parameter space (not shown). Next in importance was the transient sodium current, Nat, which was critical for regulating AP related features together with KAf (Figure S5). For this reason, our first virtual drugs were constructed by modulating each of these conductances. We applied these virtual drugs to each HD model instance in the HD PoM by changing parameters according to the virtual drug and measured the outcome in the 3D feature space of passive membrane voltage, membrane resistance and rheobase. By way of example, when Nat was modulated, we first calculated the difference between the means of the WT and the HD PoM's 'Nat' conductances, which we used as a reference perturbation in constructing the first virtual drug vd_Nat. The relative magnitude and direction of this reference perturbation is represented in Figure 4A as the mean conductance of the HD PoM's parameters after applying (i.e., adding) the reference perturbation to each. We calculated this mean conductance (1.47 for g_{Nat}) by dividing the mean of the perturbed HD PoM's parameters by the mean of the HD PoM's parameters (virtual drug-modulated parameters are shown relative to the original HD mean parameters). The virtual drug vd_Nat was then applied to each model in the HD PoM at four fractional doses, i.e., percentages of the full reference perturbation (100%, 75%, 50%, and 25%; Figure 4C). KAf conductance of the HD PoM was similarly modulated by the second virtual drug vd_KAf (Figures 4B and4D). The resulting phenotypic recovery in 3D feature space in response to vd_Nat at these doses is shown in Figure 4C, and in response to vd_KAf in Figure 4D. As shown in this figure, vd_Nat did not recover the HD phenotype, which was not surprising, since Nat was not identified as contributing to variation among the membrane excitability features in the PoM. In contrast, vd_KAf was sufficient to transform the HD PoM toward the WT PoM. We quantified the extent of efficacy and recovery of the HD PoM, summarized using four metrics (See STAR Methods). vd_Nat performed more poorly than vd_KAf in recovering the Euclidean distance in 3D, and Wasserstein distance in 3D and 7D. In contrast, vd_KAf at 100% dose recovered the Euclidean distance by at least 60% across all features and >75% in the

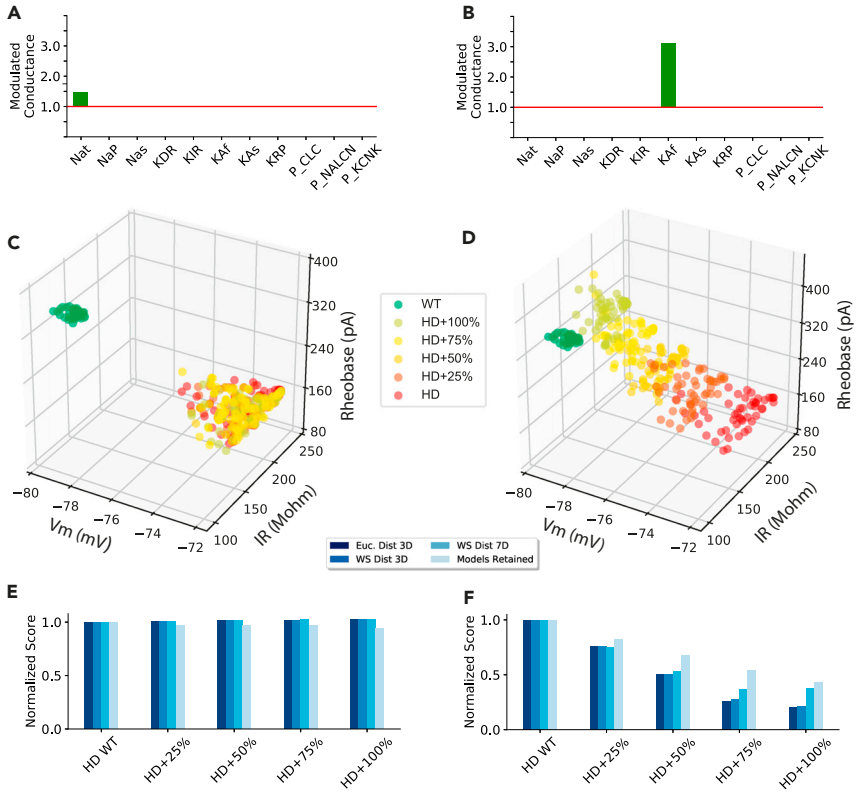

Figure 4. Single target modulation performance metrics

(A) Single target perturbation to Na^+ transient conductance (Nat) applied to the HD PoM (vd_NAT).

(B) Perturbation of fast inactivating potassium conductance (KAf) applied to the HD PoM (vd_KAF).

(C) Phenotypic recovery in three-dimensional feature space with perturbation vector shown in (A).

(D) Phenotypic recovery with perturbation vector shown in (B).

(E) Four metrics (see color key) score vd_NAT efficacy for recovering the WT PoM's phenotypes from the HD PoM's phenotypes: Euclidean and Wasserstein distance in 3 dimensions, Wasserstein distance in 7 dimensions (see STAR Methods), as well as Models Retained. "Models Retained" refers to models whose features remain within a permissible range of realistic behaviors of MSNs (feature values of the model adheres to the ranges for spiking constraints listed in Table 2, also excluding models for which automated feature extraction failed) after the perturbations are applied at each of the four intermediate doses.

(F) Same as (E) but scoring vd_KAF.

three passive membrane features, but it failed to address the heterogeneity with the HD PoM and resolve its divergence relative to the less diverse WT PoM, shown by a smaller reduction in normalized Wasserstein distance than normalized Euclidean distance in Figure 4F. Also, vd_KAf applied at higher doses understandably generated excess risk of altering other membrane properties, to the extent of breaking the response of the model, such that resulting features could not be measured. We quantified this effect with an auxiliary measure of the proportion of models retained (i.e., models producing reasonable spiking activity after virtual drug application), which decreased as vd_KAf dose increased, resulting in retention of only 40% of models at the reference dosage. It will be interesting to examine this model-based risk's relationship to toxicity measures of real CNS drugs in subsequent work.

Multiple target modulation

There has been a shift away from the "one drug, one target" approach, wherein highly potent and specific *single-target* treatments were preferred to polypharmic drugs, as they purported to mitigate off-target side effects. However, translatability from *in vitro* drug effects to *in vivo* efficacy was poor with this approach (Talevi, 2015; Rodrigues and Wild, 2017). While single target strategies appeared reasonable for known disorders controlled by single targets, such as in cardiac arrythmias (Roukoz and Saliba, 2007), neurological diseases involve disruption of network homeostasis (Ramocki and Zoghbi, 2008) and breakdown of multiple

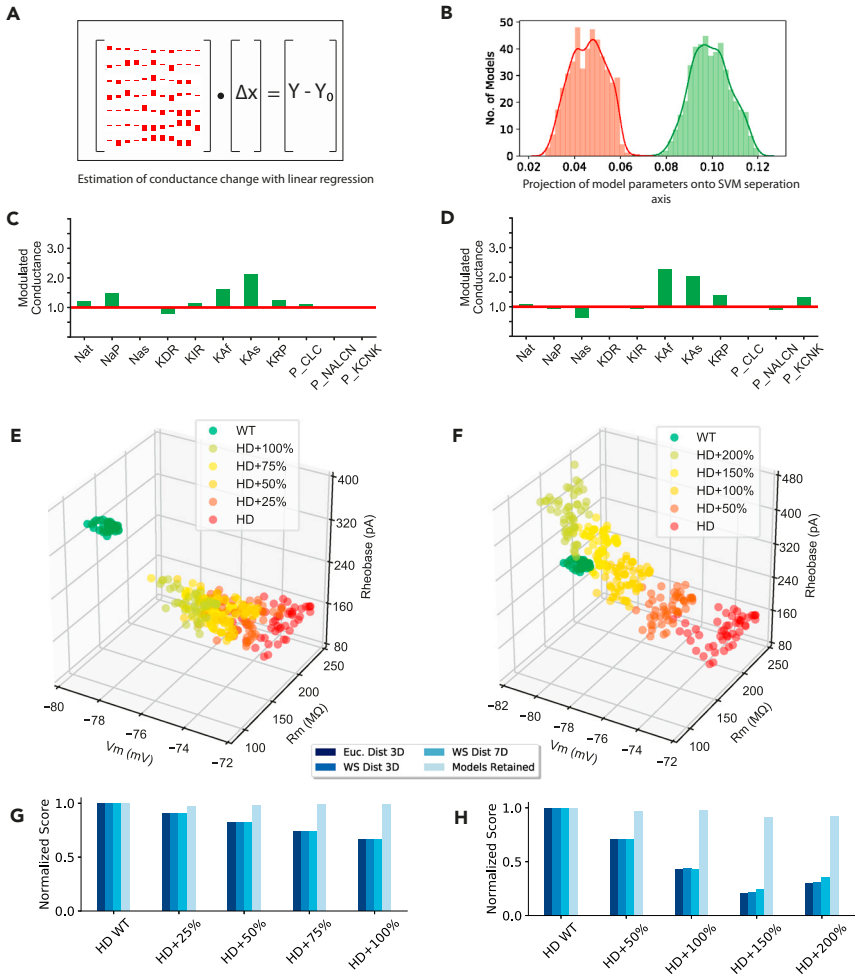

Figure 5. Multiple target modulation performance metrics using linear methods

(A) Linear Regression method used to determine conductance change for expected feature change ($Y\text{-}Y_0$).

(B) WT and HD models separated by a hyperplane determined using linear support vector machine method.

(C and D) Modulated conductance by perturbation vectors determined from method described in (A) (vd_LIN) and (B) (vd_SVM).

(E) and (F) Phenotypic recovery in three-dimensional feature space with perturbation vectors shown in (C) and (D). Note the difference in dosage for F (see text).

(G and H) Four metrics used for scoring the virtual drug's perturbation efficacy in terms of its ability to recover the HD PoM in Euclidean distance and divergence (Wasserstein distance) when applied with vd_LIN and vd_SVM at four intermediate doses.

contributing underlying biochemical cascades. For this reason, we aimed to augment polypharmic approaches with our reverse screen and identify highly potent and specific, *multi-target* treatments to alleviate complex phenotypes by the simultaneous modulation of multiple ion channels.

Linear methods sufficient to recover phenotype

Next, we considered whether it might be possible to modulate multiple parameters simultaneously and more efficiently perturb the HD models toward the WT phenotype to achieve better recovery than accomplished by our single parameter modulations. Linear regression analysis (see also supplemental information) provided insights into how multiple conductances regulated different electrophysiological properties. These linear relationships engaged multiple ionic conductances, supporting the idea that to regulate a specific feature in a desired manner, multiple conductance parameters should be perturbed simultaneously. A schematic representation of how this perturbation is determined for the HD PoM is illustrated in Figure 5A (See STAR Methods for details on its construction). To explore a second method for

constructing a multiple parameter virtual drug, we employed a linear SVM classifier to define a separating axis orthogonal to the hyperplane classification boundary. The projection of the PoMs' parameter vectors onto the separation axis determined by the SVM classifier then generated a set of values (i.e., 'scores' of arbitrary units), histograms of which together with kernel density estimation results are shown in Figure 5B. These histograms illustrate the clear separation between the two PoMs. A similar approach using logistic regression (i.e., the 'characteristic direction' method) was used previously to identify similarities and dissimilarities between gene expression studies from multiple experiments, when the underlying parameter space is high dimensional (Clark et al., 2014).

First, we calculated a reference perturbation from the linear regression analysis described in STAR Methods. The conductance vector determined by the regression (the linear solution 'X' in Figure 5A) represents the conductance changes necessary to effect the feature changes from the HD to the WT PoM (the right hand side 'Y-Y_0' in Figure 5A). We used this conductance vector's magnitude and direction as the reference perturbation for the third virtual drug vd_LIN. The relative perturbation is represented in Figure 5C as the mean conductances of the perturbed HD PoM after applying (i.e., adding) the reference perturbation to each HD model. The virtual drug vd_LIN was also applied to each model in the HD PoM at additional fractional doses, as above. The resulting phenotypic recovery in 3D feature space in response to vd_LIN at these doses is shown in Figure 5E.

Next, we calculated a reference perturbation along the separation axis of the SVM analysis described in STAR Methods. This axis is defined by a conductance vector, which is normal to the hyperplane and has a magnitude (1.12) related to the distance between the *Z* score normalized parameters of the HD and WT PoMs. Specifically, the conductance vector represents the conductance changes necessary to transform the HD PoM's parameters (in the direction of the WT PoM's parameters), such that the SVM classifier's accuracy is reduced by 50%, and to alter the model scores of the HD PoM (xaxis panel 5B) by 0.05 (arbitrary units), as required to classify them as WT PoM. We used this conductance vector's magnitude and direction for the reference perturbation of the fourth virtual drug vd_SVM. The relative perturbation is represented in Figure 5D as the mean conductance of the HD PoM's conductance parameters after applying (i.e., adding) the reference perturbation to each. The virtual drug vd_SVM was then applied to each model in the HD PoM at fractional doses ranging from 50 to 200%. The resulting phenotypic recovery in 3D feature space in response to vd_SVM at these doses is shown in Figure 5F.

While vd_LIN at maximum dose only recovered 34% of the Euclidean distance measures of the HD PoM, vd_SVM at the 150% dose recovered 80% of these measures (Figures 5G and5H). The further incremental dose (200%) of vd_SVM moved the PoM away from the WT PoM and worsened the recovery in terms of our distance metrics. As with single target modulation, both approaches failed to reduce the Wasserstein distance metric, and therefore suffered from an inability to resolve the full cohort of our HD PoM's members' dysfunctions, while resolving only the PoM's mean response metrics.

Virtual drug with heuristic approaches provided best phenotypic recovery

To address the divergence from the target WT PoM phenotype of the HD PoM phenotype after a virtual drug treatment was applied, we explored the direct use of differences between individuals for each pair of members sampled from the WT PoM and HD PoM to construct virtual drugs. We calculated the distribution of parametric differences between each HD model and each WT model, which we reasoned could supply the necessary modulation needed to yield an effective transformation of the PoM. Our first approach (Figure 6A) estimated the most frequently occurring difference vector between the two PoMs. We constructed a multidimensional histogram (illustrated for only 2 parameters in Figure 6A) over all parameter differences between members of the WT and HD PoMs (top left) and found the mode of this distribution. We formulated a second related approach by calculating the differences between the mean WT PoM's and HD PoM's parameters for each parameter independently, as shown in Figure 6B. While the former method estimates the required perturbation based on every possible parameter difference between all pairs of models across the two PoMs, the latter method estimates a direction in parameter space from the mean values of the WT and HD PoMs' parameters. Figures 6C and 6D represent the mean conductances achieved by the multiple target virtual drugs vd_HIST and vd_DIFF, applied to the HD PoM. The approaches are similar in their target modulation profile with subtle changes around modification to NaS, KIR and KCNK parameters. Both altered transient sodium and fast inactivating potassium conductances in similar relative proportions, along with NaS and KRP, resulting in feature transformations among

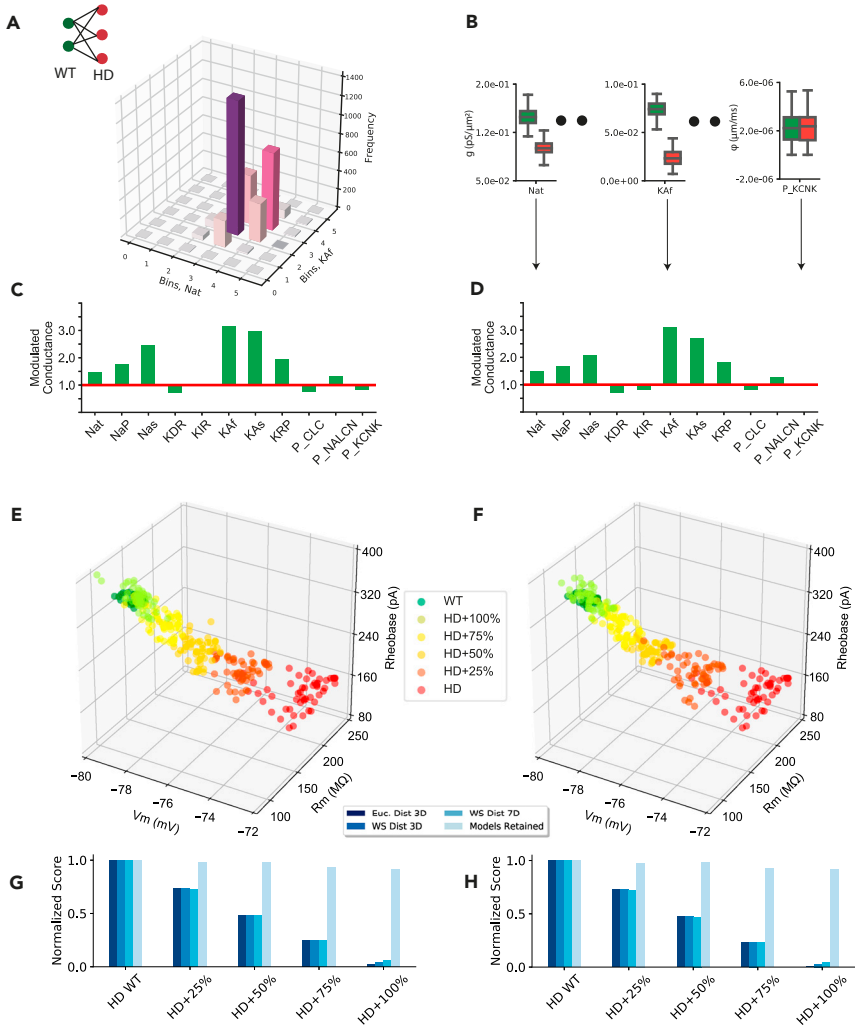

Figure 6. Multiple target modulation performance metrics using heuristic methods

(A) Multidimensional histogram (shown for only two parameters) of all possible parametric differences between WT and HD PoMs (top left).

(B) Individual parametric differences between the means of the PoMs.

(C and D) Conductance modulations by perturbation vectors determined from method described in (A) (vd_HIST) and (B) (vd_DIFF).

(E and F)Phenotypic recovery in three-dimensional feature space with perturbation vector shown in (C) and (D).

(G and H) Four metrics used for scoring the virtual drug's perturbation efficacy in terms of its ability to recover the HD PoM in Euclidean distance and divergence (Wasserstein distance) when applied with vd_HIST and vd_DIFF at four intermediate doses.

the HD PoM that were remarkably good. Not only did these virtual drugs move the HD PoM to its closest proximity to the WT PoM, but at intermediate dosages, they effected a progressive decrease in the HD PoM's members Wasserstein distance to the WT PoM. This category of virtual drug perturbation was therefore unique in its simulated efficacy (Figures 6E and 6F), and thus represents a novel approach to virtual drug design. Having addressed our most stringent criteria governing efficacy (Figures 6G and 6H), these drugs performed surprisingly well and therefore warrant further investigation for designing therapeutics for HD and other disorders with similar cellular disease phenotypes.

Triaging approach using virtual drugs to design efficient target modulation

We further compared performance metrics among all the virtual drugs used in this study. First, we examined the extent of recovery in the distributions of all features. As illustrated in Figure 7A, feature

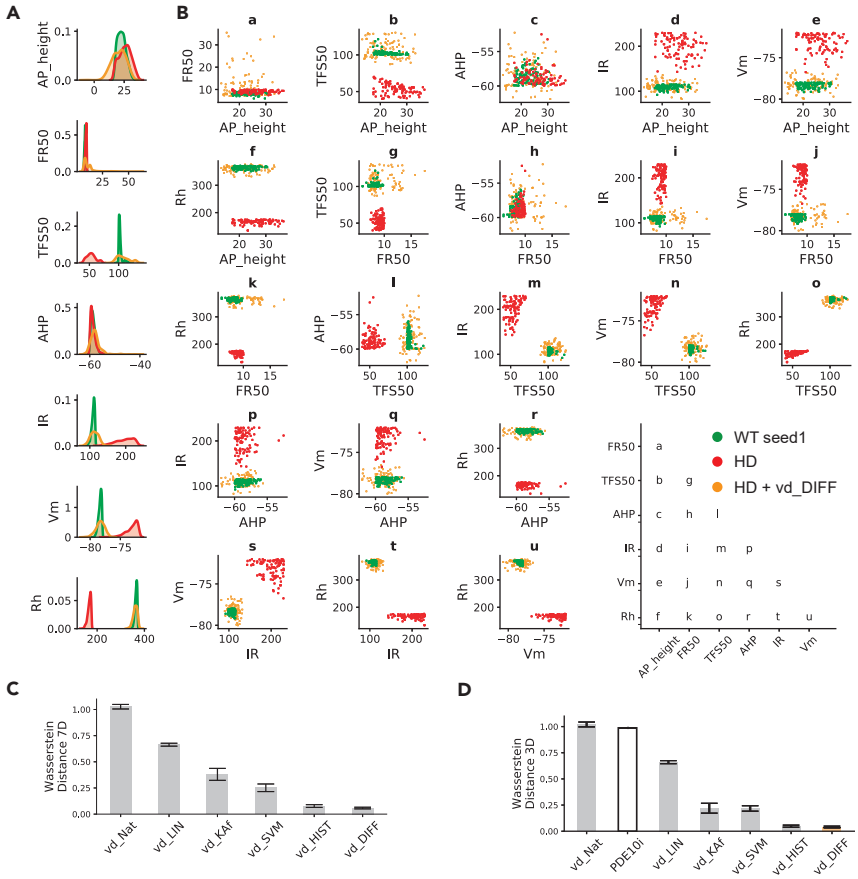

Figure 7. Validation and performance metrics of virtual drugs

(A) Kernel density estimates show full recovery of the HD PoM (red) when perturbed with the best virtual drug (orange) and overlap the WT PoM (green).

(B) Pairwise scatterplots of all features. The best virtual drug, vd_DIFF, recovered spiking features that were added in this study, and which extended previous empirical measures of excitability.

(C) Drug scores calculated from the averages of four metrics (Figures 4, 5, and 6) for each virtual drug at their best dosage identified in this study.

(D) Drug scores calculated from the average of two metrics (Wasserstein distance in 7 and 3 dimensions) allowing comparison across each the virtual drugs at best dosage and the real drug, PDE10i.

distributions of the HD PoM (red) appear disjoint from the WT PoM (green), but appear proximal to the WT PoM (green) when perturbed with the best virtual drug vd_DIFF (orange). Figure 7B provides a visual representation of the rescue of WT phenotype across all feature pairs. As seen in subplots s, t and u for pairwise combinations of V_m, IR and Rh, the virtual drug vd_DIFF also addressed the divergence in distributions from HD to WT. However, for features such as FR50 and TFS50, the vd_DIFF treated HD PoM distributions exhibited a wider resulting spread. These results allude to possible next generation model enhancements beyond the current single compartment approximation using ionic conductances alone, such as optimizing ion channel parameters governing activation and inactivation kinetics and time constants. Additional structural complexity, such as dendritic compartments, may also be required to address these features.

We note that virtual screening and scoring methods in traditional drug discovery are mostly centered around estimating ligand-protein binding affinities and energies (McInnes, 2007). Scoring drugs based on their ability to address recovery in terms of population heterogeneity and divergence has remained unexplored prior to our study. Here, we have introduced a novel screening method to quantify drugs' efficacy not just in terms of recovering single models or a population mean, but also based on their ability to resolve a heterogeneous PoM's multidimensional phenotype, representative of the full contingent of cellular phenotypes and their joint distributions occurring in the target tissue. We scored virtual drugs from the average

of four metrics (See STAR Methods and Figures 4, 5, and 6). The virtual drug vd_DIFF performed best, followed closely by vd_HIST, each of which recovered ~70% of the total WT-HD distance. We also compared these drugs in two metrics, Euclidean and Wasserstein distance, for three passive membrane properties (Figure 1) and found similarly high efficacy.

Lastly, recalling the performance of PDE10i from Figure 1, wherein the drug only recovered 27% of the Euclidean distance metric constructed from the three passive membrane properties in the empirically observed WT and HD data, we note that the majority of our virtual drugs performed better in rescuing the WT phenotypes (Figure 7D).

DISCUSSION

Motivation

In contrast to traditional target-based drug discovery strategies, which identify and validate specific molecular targets, phenotypic drug discovery strategies focus on first collecting physiologically relevant endpoints and then probing for underlying molecular targets in an agnostic manner, thus diminishing target validation risk (Moffat et al., 2017). With more first-in-class drug discoveries being made from such phenotypic drug discovery strategies, a huge opportunity lurks in developing screening tools that enable decision making on the viability of compounds along their well-known multidimensional paths from disease and risk to health and safety, and ultimately for fostering successes in the development of therapies for CNS disorders among the current drug development pipeline.

HD phenotypes

Our study began with the assumption that the underlying variability of neuronal electrophysiological phenotypes in HD arises from differential modulation of ion channel conductance densities across principal neurons in the tissue most affected by HD, the striatum. Evidence also points to other sources of variability associated with MSN dysfunction beyond somatic ionic conductances, such as morphological alterations of dendritic topology (Goodliffe et al., 2018) modulation of extracellular K^+ levels contributed by K^+ channel dysfunction among astrocytes (Tong et al., 2014), TrkB signaling pathway modification of K^+ channel interacting protein KChIP with Kv4.2 channel subunits (Carrillo-Reid et al., 2019), alterations to synaptic and receptor function (Raymond et al., 2011). Other theoretical and modeling studies further corroborate experiments showing disruptions to the balance between excitatory and inhibitory inputs within striatal networks (Ponzi et al., 2020). Kinetic parameters of ion channel models' sub-threshold voltage gating mechanisms were not varied in this study, though the coregulation of channel kinetics provides general mechanisms for regulating neuronal excitability (McAnelly and Zakon, 2000). Prior immunohistochemical studies in MSNs from transgenic mice associated the reduction in inward and outward K^+ conductances, and expression of specific K^+ channel subunits, to altered active and passive membrane properties in HD model animals (Ariano et al., 2005). Despite these potentially confounding variables, by varying only maximum conductance parameters our study produced PoMs that closely matched experimental data and provided key methods for measuring drug efficacy and designing multi-target virtual drugs. To summarize our findings:

i) Our model-based observations show how reduced K^+ channel expression can sufficiently alter neuronal excitability (Figures 3, 4, 5, 6, 7, S3, and S4) to explain observations that voltage gated K^+ channels influence membrane depolarization and control striatal neuron firing (Hopf et al., 2003).

ii) In our models, fast and slow inactivating A-Type K^+ conductances are greatly modified, which contributed to the difference in somatic excitability among WT and HD PoMs' phenotypes (Figures 4, 5, and 6). However, prior evidence of fast inactivating K^+ channel Kv4.2 dysfunction was localized to the distal dendrites of D2-type MSNs (Day et al., 2008). Contrary to our findings, in these studies, Kv4 current was elevated to make the dendrites hypoexcitable, which occurred alongside decreased cortical drive, through impaired TrkB signaling. We propose that somatic excitability may be an additional homeostatic response to decreased efficacy of cortical drive. This hypothesis requires further experimentation to test, wherein the non-homogenous distribution profile of these ion channels is probed to examine if indeed Kv4.2 are differentially modulated in HD among soma and distal dendrites.

iii) Our parametric analysis of the PoMs revealed a decrease in slowly inactivating K^+ conductance, which substantiates prior evidence revealing downregulation of Kv2.1 channel expression (Ariano

et al., 2005). Several types of K^+ channel subunits identified, including Kv1.4, Kv4.2, Kv2.1 (Sheng et al., 1992) give rise to slowly inactivating currents. Most likely, the strongest reduction in A-type among the HD PoM, fast and slow inactivating K^+ and persistent K^+ conductances (Figures 3, S4, and S5), could be attributed to their crucial role in delaying threshold excitation in the model (TFS feature used in this study) in response to injected current, which captures a key characteristic of MSNs. We imposed a stricter constraint on WT models to reproduce this feature with TFS>100ms, which may have caused these currents to be strongly upregulated in the WT PoMs. Furthermore, channel engagement at the different phases of membrane excitation during sub-threshold membrane depolarization contributes differentially to this characteristically delayed excitation (Surmeier et al., 1988; Nisenbaum et al., 1996).

iv) In our models, a transient Na^+ conductance required upregulation in order to rescue the HD phenotype. Though there is no direct evidence to our knowledge of reduced expression of the Nav1.2 channel in HD, evidence that sodium channel β4 subunit downregulation in HD transgenic animals may underlie neuritic degeneration does exist (Oyama et al., 2006). In fact, among cultured cerebellar granule cells, knockdown of Navβ4 (Scn4b) revealed the loss of resurgent current, reduced persistent current, and a downward shift in half-inactivation voltage of transient current, thus altering firing patterns. Though, our findings do not establish a direct link to the upstream genetic pathways, increasing Na^+ currents alone was not sufficient to rescue cell excitability of HD phenotypes (Figure 4C).

v) Our models reveal that KRP and NaS were strongly correlated in both WT and HD phenotypes in order to maintain targeted firing properties (Figures 3B, S4, and S5). NaS is a TTX insensitive Na^+ current and is a known target for modulation of neuronal firing properties (Hoehn et al., 1993), while persistent components of the total K^+ current were pharmacologically heterogeneous, being available over a broad range of membrane potentials (Nisenbaum et al., 1996). It is not surprising that these two currents were strongly implicated in maintaining firing rates across the PoMs.

vi) Surprisingly, the KIR conductances in our HD models were upregulated for this model population, while prior evidence attributed hyperexcitability of D2 MSNs from HD model animals to reduced KIR currents. We believe this finding was due to the limitations of the protocols we employed for modeling hyperpolarizing current injections, which may have been insufficient to engage KIR conductance modulation of membrane properties to the same extent as experimental protocols (Zhao et al., 2016; Sebastianutto et al., 2017). When using alternate WT populations established from different seeds (FiguresS4 and S5), we did observe a need to upregulate KIR conductance to recover the WT PoMs.

vii) We observed differences between the WT and HD model phenotypes with respect to specific leak components. We note that replacing the original nonspecific linear leak model with a set of specific nonlinear leak components (see STAR Methods) was appropriate for overcoming a major drawback of 'Mahon et al., model' (Mahon et al., 2000), i.e., the use of different reversal potentials (E_K or E_{Na}) for each model channel conductance. Without this modification, biophysical interpretation of the model would be impossible. Secondly, not separating the leak components would likely have led the optimization of membrane depolarization toward finding solutions that relied on modulating this leak component, at which point it would be difficult to interpret the biophysical substrate and associated targets for such a lumped leak component. In our study, we observed mixtures of specific leak components within our virtual drug specifications, introducing some degeneracy to potential solutions for transforming HD models into WT, as potentially different combinations of specific leak modulations could equally be used. However, these solutions are less degenerate than if we had performed these simulations with a single leak component, as a single leak conductance value may correspond to any combination of ion-specific leak conductances. Additionally, modeling work and concomitant patch clamp recordings in Purkinje neurons revealed that GHK-based leak models followed a nonlinear I-V relationship and are better at predicting the nonlinear voltage responses to current injections (Huang et al., 2015).

Network effects and dichotomous MSN types

An important additional consideration not included in this modeling study is the distinction between different classes of MSNs. Previous studies attributed intrinsic excitability differences to dichotomous D1 and D2-type dopamine receptors (D1Rs and D2Rs), which modulate the corresponding classes of MSNs and affect how they integrate synaptic inputs differently (Gertler et al., 2008). While dopamine's

regulation of KIR channels in D1-type MSNs enhances resonant frequency and reduces resonant impedance, its effect on D2-type MSNs is the opposite. Each receptor type engages different subcellular biochemical cascades, with D1Rs acting via cAMP-PKA signaling, and D2Rs modulating KIR channels through PLC-PKC signaling (Zhao et al., 2016). These important considerations will drive future studies in which D1-type and D2-type MSN phenotypes are represented in PoMs. Also, striatal network connectivity is greatly disrupted in transgenic animals, including alterations to presynaptic compartments and network activity. Recent studies highlighting the pre-synaptic sources of dysfunction to alter network dynamics and microfluidic platforms to investigate such mechanisms will be very valuable to drug design (Virlogeux et al., 2018) in addition to the methods described here.

Virtual drug translation

Ex vivo evaluations supported the notion that dysregulation of cyclic nucleotide signaling can be restored with PDE10i (Padovan-Neto et al., 2015). In the symptomatic HD mouse models Q175 and R6/2, cyclic nucleotide dysregulation contributes to neurophysiological dysfunction. PDE10i reversed hyperexcitability of MSNs, both *in vivo* and *in vitro*, while also elevating cAMP levels. One particular compound, PF-02545920, a selective PDE10A inhibitor (Beaumont et al., 2016), failed to meet the clinical endpoint of alleviating motor symptoms despite its success at addressing preclinical HD deficits (Beaumont et al., 2016). The current study aimed to provide a quantitative measure of how well the drug addressed the recovery of *in vitro* electrophysiological properties in the multidimensional measurement space of MSN phenotypes, as independent statistical comparisons across three features may not have been sufficient to assess joint distributions and therefore accurately predict the clinical performance of the drug. We introduced the multidimensional metric, Euclidean distance measured in 3D, and we aimed to recover a heterogeneous population according to divergence measured in an extended metric space (Figure 1). We set stringent criteria for recovery of the HD PoM's phenotype into a narrow heterogeneous WT region of feature space. Using virtual drugs, we modulated the underlying model parameters and thus introduced novel standards of defining effective phenotypic recovery for both virtual and real drugs.

Though by no means trivial, identifying ideal drug compounds or drug combinations that target multiple ion channels, such as those found among our multidimensional targets, is in fact feasible given that screening methods in medicinal chemistry are capable of testing precise modulation profiles. We have identified and presented here methods to compare these profiles against ideal virtual drug profiles (Figures 7C and 7D). We also propose searching known drug interaction databases for potential novel compounds that target proteins whose modulation is correlated with elements of our perturbation vectors (i.e., ionic conductance modulation ratios). Finding combinations determined by simple vector arithmetic, a match to the perturbation profile of our best virtual drugs (Figures 7C and 7D) becomes possible. The first step for accomplishing this is to map required changes for each ionic conductance (i.e., elements of the perturbation vector) to an equivalent drug dose via the IC_{50}/EC_{50} responses of drugs targeting each channel current. In cardiac electrophysiology simulations for pro-arrhythmic safety testing, drug-block within models is achieved by scaling the maximum conductance of an affected ion channel using IC_{50}/EC_{50} scaling factors (Mirams et al., 2012). If these values were well cataloged for neuronal ion channels, our proposed virtual drugs could potentially be transcribed into sets of multi-compound therapeutics that are predicted to maximize phenotypic recovery. In the current study we modulate intrinsic membrane conductances of single neurons, so the conclusions we draw around potential therapeutics are limited to those that have an effect upon such properties. However, we believe that in extensions of this work, systems at different scales or involved in other neural processes can be simulated in WT and disease conditions, to match data from other pre-clinical sources, and the analytical methods proposed here would still be capable of facilitating the discovery of therapeutics in those related areas using more complex simulations.

Multi-scale extensions

Unlike in cardiac electrophysiology, where ion channel dysfunction sufficiently explains phenotypic variability (Lawson et al., 2018), in neuronal electrophysiology, evidence points to sources of phenotypic variability arising from dendritic topologies, network topologies, and subcellular mechanisms. Since striatum constitutes multiple neuron types, and prior studies showing altered FSI firing is sufficient to disrupt balanced firing between D1-type and D2-type MSNs (Damodaran et al., 2014), incorporation of these mechanisms will greatly enhance confidence around the 'virtual drug' profile's ability to target network phenotypes. Our neuronal optimization framework does not restrict construction of such topologically constrained large-scale brain architectures, as its constituent Neural Tissue Simulator is built to handle

simulations of high order components, for example, a million neurons and a billion synapses (Kozloski and Wagner, 2011). A preceding study from our group, using the same optimization methods, employed a model that included dendrites and novel dimensionality reduction techniques to identify metaparameter controllers of sub-threshold oscillations and spontaneous firing in dopamine neurons from a 36-dimensional parametric space (Rumbell and Kozloski, 2019). Somatic or dendritic conductance changes determined from single neuron analyses can therefore be easily extended into network architectures to design future studies targeting network activity as a phenotype (Ponzi et al., 2020). Finally, with highly parameterized models, careful consideration will be made toward uncertainty quantification of the model parameters in estimating qualitative output behaviors (Eriksson et al., 2019).

Conclusions

We have developed a reverse phenotypic screening method to identify the 'ideal' virtual perturbation underlying ion channel targets to rescue a heterogeneous population of HD models' neuronal excitability phenotype to WT. Our approach is based on quantitative systems pharmacology principles and combines mechanistic simulations, generation of populations of models, and statistical screening approaches for early validation of virtual drug candidates. First, by building databases of neuron models representing both healthy and disease phenotypes we provided mechanistic insights into how ionic conductance parameters influence the varied electrophysiological properties that gave rise to distinct clusters of phenotypes. Second, we described several approaches using statistical and machine learning methods to perform reverse phenotypic screening and design single target and multiple target perturbations for rescuing a heterogeneous disease population to the healthy phenotype. We also introduced several metrics to compare the performance of the virtual drug perturbations with a failed pharmacotherapy using PDE10i in HD. These screening approaches provide novel tools for drug design when complemented with directed *in vitro* electrophysiological studies for preclinical validation of drug targets.

With increasing cost of clinical trial failure in the domain of nervous system disorders and a paradigm shift in drug discovery toward automated high-throughput screening platforms, our approaches can become an important part of the evaluation of drug action on underlying physiology. As multi-parametric subcellular responses are regularly measured using multiple data streams, from gene expression studies to human-derived iPSC electrophysiological recordings, we anticipate that these concepts and methods will become even more relevant to drug development and its movement toward provisioning of patient-specific precision therapies (Mirams et al., 2012).

Limitations of study

The primary limitation of the methods introduced here to identify virtual drug candidates is that they were designed under the assumption of unimodal parameter distributions within the HD and WT PoMs. For example, the best performing virtual drug, vd_DIFF, was calculated using the difference between the means of two PoMs, a measurement that may be largely meaningless if one of the PoMs is highly multimodal. Ideally, the PoMs generated for the phenotypic conditions of interest would stem from a broad unimodal distribution across the majority of empirically observed feature space. This indeed was the case in the current study for our initial optimization targeting the 3 empirical features (Figure 2A). However, for our refined optimization that constrained the modified Mahon et al. (2000) model (see STAR Methods) to match multiple passive as well as spiking membrane potential criteria, across each of several optimization trials using different random seeds, and targeting specific subregions of feature space, our model samples were generated from narrow distributions representing disjoint local minima from across the target feature space (see results section "Population of models for characterizing WT and HD electrophysiological phenotypes", and supplemental information for details). Despite downsampling to attempt to match the empirical distribution as closely as possible (see supplemental information), we were unable to avoid a highly multimodal WT PoM. Virtual drug generation methods for multi-modal distribution of models is beyond the scope of this paper. Instead, we show how the methods described are generally applicable to modes with low error (e.g., Modes B and F). The parameters of models from Modes B and F (Figure S3) are quite distinct from those from Mode A presented in the main section of the paper (Figure 3). As such, we instead selected a single optimization trial result to use for analysis and chose the WT PoM with the largest Wasserstein distance from the HD PoM as the target, thereby taking on the most challenging available unimodal phenotypic recovery task. Testing the vd_DIFF method with other WT PoMs, we found comparable phenotypic recovery to that reported in the results (Figure S5). We conclude that each discovered WT

unimodal PoM would result in a different optimal virtual drug candidate, and that selection of the most promising or desirable from among these possible candidates would be based either on user preference, constraints on drug development, or additional analyses. Additionally, accounting for homeostatic mechanisms, and optimization objectives to minimize toxicity risk when adding the virtual drugs to the WT PoMs will be critical. Finally, pooling populations from multi-objective optimization results could result in highly multimodal distributions in parameter or feature space, and the handling of such scenarios will therefore require further development of the methods presented here. In optimization studies, ensuring that all possible candidate solutions to a problem are found is a known challenge, especially within a high-dimensional and complex parameter landscape, making results of our virtual drug development methods dependent on optimization metaparameters. Therefore, future studies will need to focus on ensuring that all viable parameter regions are discovered. State-of-the-art advances in solving stochastic inverse problems for mechanistic models (Parikh and James Kozloski, 2020) may provide a path toward this previously challenging goal with further development of the methods presented here.

One caveat to the interpretation of some of our results from the models is the existence of degenerate solutions of complex systems (Edelman and Gally, 2001). Such solutions have been demonstrated in prior experimental and theoretical studies in neurons, where multiple solutions of ion channel conductances produce similar neuronal excitability phenotypes (Marder and Taylor, 2011; Goaillard and Dufour, 2014). If one channel is deleted, the excitability can still be maintained by other compensatory mechanisms. It is therefore likely that using a different biophysical model of the MSN with more dendritic complexity and ionic conductances contingent upon neuronal topology, such as the Wolf model (Wolf et al., 2005) would reveal alternate virtual drugs and create a more complete reverse screen for recovery. These predictions require further validation in models constrained by detailed preclinical measurements, but do not undermine the applicability of our methodology to drug design given appropriate models and appropriate preclinical datasets.

STAR★METHODS

Detailed methods are provided in the online version of this paper and include the following:

- KEY RESOURCES TABLE
- RESOURCE AVAILABILITY
  - Lead contact
  - Materials availability
  - Data and code availability
- METHOD DETAILS
  - Model and simulations
  - Neuron model
  - Software
  - Parameter search
  - Selection of population of WT models for analysis
  - Population modeling
  - Virtual drug construction
  - Virtual drug validation on different WT population of models
- QUANTIFICATION AND STATISTICAL ANALYSIS
  - Scoring metrics
  - Sample size selection
  - Other visualization and statistical methods

SUPPLEMENTAL INFORMATION

Supplemental information can be found online at https://doi.org/10.1016/j.isci.2021.103279.

ACKNOWLEDGMENTS

All authors are employees of IBM Research. The authors would like to acknowledge CHDI Foundation and Slava Gurev for insightful suggestions for statistical analysis. We thank the reviewers for critically reading the manuscript and suggesting substantial improvements.

Funding information: Portions of the work reported here were funded by CHDI Foundation, Inc. The funders had no role in study design, data collection and analysis, decision to publish, or preparation of the manuscript.

AUTHOR CONTRIBUTIONS

SA, TR, JK wrote the manuscript. SA, TR, JK conceived the design. SA, THT developed the MSN model and TR, THT designed the optimization framework. SA performed the calculations. SA, TR, JP analyzed the data. JK was in charge of overall direction and planning. All authors reviewed the manuscript.

DECLARATION OF INTERESTS

The authors declare no competing interests.

Received: June 11, 2020
Revised: August 5, 2021
Accepted: October 13, 2021
Published: November 19, 2021

REFERENCES

Accardi, M.V., Pugsley, M.K., Forster, R., Troncy, E., Huang, H., and Authier, S. (2016). The emerging role of in vitro electrophysiological methods in CNS safety pharmacology. J. Pharmacol.Toxicol.Methods *81*, 47–59. https://doi.org/10.1016/j.vascn.2016.03.008.

André, V.M., Cepeda, C., Fisher, Y.E., Huynh, M., Bardakjian, N., Singh, S., Yang, X.W., and Levine, M.S. (2011). Differential electrophysiological changes in striatal output neurons in Huntington's disease. J. Neurosci. *31*, 1170–1182. https://doi.org/10.1523/JNEUROSCI.3539-10.2011.

Ariano, M.A., Cepeda, C., Calvert, C.R., Flores-Hernández, J., Hernández-Echeagaray, E., Klapstein, G.J., Chandler, S.H., Aronin, N., DiFiglia, M., and Levine, M.S. (2005). Striatal potassium channel dysfunction in Huntington's disease transgenic mice. J. Neurophysiol. *93*, 2565–2574. https://doi.org/10.1152/jn.00791.2004.

Beaumont, V., Zhong, S., Lin, H., Xu, W.J., Bradaia, A., Steidl, E., Gleyzes, M., Wadel, K., Buisson, B., Padovan-Neto, F.E., et al. (2016). Phosphodiesterase 10A inhibition improves cortico-basal ganglia function in Huntington's disease models. Neuron *92*, 1220–1237. https://doi.org/10.1016/j.neuron.2016.10.064.

Bowes, J., Brown, A.J., Hamon, J., Jarolimek, W., Sridhar, A., Waldron, G., and Whitebread, S. (2012). Reducing safety-related drug attrition: the use of in vitro pharmacological profiling. Nat. Rev. Drug Discov. *11*, 909–922. https://doi.org/10.1038/nrd3845.

Britton, O.J., Bueno-Orovio, A., Van Ammel, K., Lu, H.R., Towart, R., Gallacher, D.J., and Rodriguez, B. (2013). Experimentally calibrated population of models predicts and explains intersubject variability in cardiac cellular electrophysiology. Proc. Natl. Acad. Sci. U. S. A. *110*, E2098–E2105. https://doi.org/10.1073/pnas.1304382110.

Carrillo-Reid, L., Day, M., Xie, Z., Melendez, A.E., Kondapalli, J., Plotkin, J.L., Wokosin, D.L., Chen, Y., Kress, G.J., Kaplitt, M., et al. (2019). Mutant Huntingtin enhances activation of dendritic Kv4 K+ channels in striatal spiny projection neurons. eLife *8*, e40818. https://doi.org/10.7554/eLife.40818.

Clark, N.R., Hu, K.S., Feldmann, A.S., Kou, Y., Chen, E.Y., Duan, Q., and Ma'ayan, A. (2014). The characteristic direction: a geometrical approach to identify differentially expressed genes. BMC Bioinform. *15*, 1–16. https://doi.org/10.1186/1471-2105-15-79.

Coppen, E.M., and Roos, R.A.C. (2017). Current pharmacological approaches to reduce chorea in Huntington's disease. Drugs *77*, 29–46. https://doi.org/10.1007/s40265-016-0670-4.

Damodaran, S., Evans, R.C., and Blackwell, K.T. (2014). Synchronized firing of fast-spiking interneurons is critical to maintain balanced firing between direct and indirect pathway neurons of the striatum. J. Neurophysiol. *111*, 836–848. https://doi.org/10.1152/jn.00382.2013.

Day, M., Wokosin, D., Plotkin, J.L., Tian, X., and Surmeier, D.J. (2008). Differential excitability and modulation of striatal medium spiny neuron dendrites. J. Neurosci. *28*, 11603–11614. https://doi.org/10.1523/JNEUROSCI.1840-08.2008.

Deb, K., Thiele, L., Laumanns, M., and Zitzler, E. (2002). Scalable multi-objective optimization test problems. In Proceedings of the 2002 Congress on Evolutionary Computation, CEC. https://doi.org/10.1109/CEC.2002.1007032.

Dunlop, J., Bowlby, M., Peri, R., Vasilyev, D., and Arias, R. (2008). High-throughput electrophysiology: an emerging paradigm for ion-channel screening and physiology. Nat. Rev. Drug Discov. *7*, 358–368. https://doi.org/10.1038/nrd2552.

Eddy, W.F. (1977). A new convex hull algorithm for planar sets. ACM Trans. Math.Softw. *3*, 398–403. https://doi.org/10.1145/355759.355766.

Edelman, G.M., and Gally, J.A. (2001). Degeneracy and complexity in biological systems. Proc. Natl. Acad. Sci. U. S. A. *98*, 13763–13768. https://doi.org/10.1073/pnas.231499798.

Eriksson, O., Jauhiainen, A., Maad Sasane, S., Kramer, A., Nair, A.G., Sartorius, C., and Kotaleski, J.H. (2019). Uncertainty quantification, propagation and characterization by Bayesian analysis combined with global sensitivity analysis applied to dynamical intracellular pathway models. Bioinformatics *35*, 284–292. https://doi.org/10.1093/bioinformatics/bty607.

Van Geit, W., Gevaert, M., Chindemi, G., Rössert, C., Courcol, J.D., Muller, E.B., Schürmann, F., Segev, I., and Markram, H. (2016). BluePyOpt: leveraging open source software and cloud infrastructure to optimise model parameters in neuroscience. Front. Neuroinform. *10*, 17. https://doi.org/10.3389/fninf.2016.00017.

Gertler, T.S., Chan, C.S., and Surmeier, D.J. (2008). Dichotomous anatomical properties of adult striatal medium spiny neurons. J. Neurosci. *28*, 10814–10824. https://doi.org/10.1523/JNEUROSCI.2660-08.2008.

Goaillard, J.-M., and Dufour, M.A. (2014). The pros and cons of degeneracy. eLife *3*, e02615. https://doi.org/10.7554/eLife.02615.

Gong, J.Q.X., and Sobie, E.A. (2018). Population-based mechanistic modeling allows for quantitative predictions of drug responses across cell types. NPJ Syst. Biol. Appl. *4*, 1–11. https://doi.org/10.1038/s41540-018-0047-2.

Goodliffe, J.W., Song, H., Rubakovic, A., Chang, W., Medalla, M., Weaver, C.M., and Luebke, J.I. (2018). Differential changes to D1 and D2 medium spiny neurons in the 12-month-old Q175+/- mouse model of Huntington's Disease. PLoS One *13*, e020062. https://doi.org/10.1371/journal.pone.0200626.

Gouwens, N.W., Berg, J., Feng, D., Sorensen, S.A., Zeng, H., Hawrylycz, M.J., Koch, C., and Arkhipov, A. (2018). Systematic generation of biophysically detailed models for diverse cortical neuron types. Nat. Commun. *9*, 1–13. https://doi.org/10.1038/s41467-017-02718-3.

Gouwens, N.W., Sorensen, S.A., Baftizadeh, F., Budzillo, A., Lee, B.R., Jarsky, T., Alfiler, L., Arkhipov, A., Baker, K., Barkan, E., et al. (2020). Toward an integrated classification of neuronal

cell types: morphoelectric and transcriptomic characterization of individual GABAergic cortical neurons. bioRxiv. https://doi.org/10.1101/2020.02.03.932244.

Greengard, P., Allen, P.B., and Nairn, A.C. (1999). Beyond the dopamine receptor: the DARPP-32/protein phosphatase-1 cascade. Neuron *23*, 435–447. https://doi.org/10.1016/S0896-6273(00)80798-9.

Hoehn, K., Watson, T.W.J., and MacVicar, B.A. (1993). A novel tetrodotoxin-insensitive, slow sodium current in striatal and hippocampal beurons. Neuron *10*, 543–552. https://doi.org/10.1016/0896-6273(93)90341-N.

Hopf, F.W., Cascini, M.G., Gordon, A.S., Diamond, I., and Bonci, A. (2003). Cooperative activation of dopamine D1 and D2 receptors increases spike firing of nucleus accumbens neurons via G-protein βγ subunits. J. Neurosci. *23*, 5079–5087. https://doi.org/10.1523/JNEUROSCI.23-12-05079.2003.

Huang, S., Hong, S., and De Schutter, E. (2015). Non-linear leak currents affect mammalian neuron physiology. Front. Cell.Neurosci. *9*, 432. https://doi.org/10.3389/fncel.2015.00432.

Kang, M.S., Yang, Y.S., Kim, S.H., Park, J.M., Eun, S.Y., and Jung, S.C. (2014). The downregulation of somatic A-type K+ channels requires the activation of synaptic NMDA receptors in young hippocampal neurons of rats. Korean J. Physiol. Pharmacol. *18*, 135–141. https://doi.org/10.4196/kjpp.2014.18.2.135.

Klapstein, G.J., Fisher, R.S., Zanjani, H., Cepeda, C., Jokel, E.S., Chesselet, M.F., and Levine, M.S. (2001). Electrophysiological and morphological changes in striatal spiny neurons in R6/2 Huntington's disease transgenic mice. J. Neurophysiol. *86*, 2667–2677. https://doi.org/10.1152/jn.2001.86.6.2667.

Kozloski, J., and Wagner, J. (2011). An ultrascalable solution to large-scale neural tissue simulation. Front.Neuroinform. *5*, 15. https://doi.org/10.3389/fninf.2011.00015.

Kravitz, R.L., Duan, N., and Braslow, J. (2004). Evidence-based medicine, heterogeneity of treatment effects, and the trouble with averages. Milbank Q. *82*, 661–687. https://doi.org/10.1111/j.0887-378X.2004.00327.x.

Lawson, B.A.J., Drovandi, C.C., Cusimano, N., Burrage, P., Rodriguez, B., and Burrage, K. (2018). Unlocking data sets by calibrating populations of models to data density: a study in atrial electrophysiology. Sci. Adv. *4*, e1701676. https://doi.org/10.1126/sciadv.1701676.

Mahon, S., Deniau, J.M., Charpier, S., and Delord, B. (2000). Role of a striatal slowly inactivating potassium current in short-term facilitation of corticostriatal inputs: a computer simulation study. Learn. Mem. *7*, 357–362. https://doi.org/10.1101/lm.34800.

Marder, E. (2011). Variability, compensation, and modulation in neurons and circuits. Proc. Natl. Acad. Sci. U. S. A. *108*, 15542–15548. https://doi.org/10.1073/pnas.1010674108.

Marder, E., and Taylor, A.L. (2011). Multiple models to capture the variability in biological neurons and networks. Nat. Neurosci. *14*, 133–138. https://doi.org/10.1038/nn.2735.

McAnelly, M.L., and Zakon, H.H. (2000). Coregulation of voltage-dependent kinetics of Na(+) and K(+) currents in electric organ. J. Neurosci. *20*, 3408–3414.

McInnes, C. (2007). Virtual screening strategies in drug discovery. Curr.Opin. Chem.Biol. *11*, 494–502. https://doi.org/10.1016/j.cbpa.2007.08.033.

Mirams, G.R., Davies, M.R., Cui, Y., Kohl, P., and Noble, D. (2012). Application of cardiac electrophysiology simulations to pro-arrhythmic safety testing. Br. J. Pharmacol. *167*, 932–945. https://doi.org/10.1111/j.1476-5381.2012.02020.x.

Moffat, J.G., Vincent, F., Lee, J.A., Eder, J., and Prunotto, M. (2017). Opportunities and challenges in phenotypic drug discovery: an industry perspective. Nat. Rev. Drug Discov. *16*, 531–543. https://doi.org/10.1038/nrd.2017.111.

Möller, C., and Witchel, H. (2011). Automated electrophysiology makes the pace for cardiac ion channel safety screening. Front. Pharmacol. *2*, 73. https://doi.org/10.3389/fphar.2011.00073.

Nisenbaum, E.S., Wilson, C.J., Foehring, R.C., and Surmeier, D.J. (1996). Isolation and characterization of a persistent potassium current in neostriatal neurons. J. Neurophysiol. *76*, 1180–1194. https://doi.org/10.1152/jn.1996.76.2.1180.

Obergrussberger, A., Stölzle-Feix, S., Becker, N., Brüggemann, A., Fertig, N., and Möller, C. (2015). Novel screening techniques for ion channel targeting drugs. Channels *9*, 367–375. https://doi.org/10.1080/19336950.2015.1079675.

Octeau, J.C., Gangwani, M.R., Allam, S.L., Tran, D., Huang, S., Hoang-Trong, T.M., Golshani, P., Rumbell, T.H., Kozloski, J.R., and Khakh, B.S. (2019). Transient, consequential increases in extracellular potassium ions accompany channelrhodopsin2 excitation. Cell Rep. *27*, 2249–2261.e7. https://doi.org/10.1016/j.celrep.2019.04.078.

Oyama, F., Miyazaki, H., Sakamoto, N., Becquet, C., Machida, Y., Kaneko, K., Uchikawa, C., Suzuki, T., Kurosawa, M., Ikeda, T., et al. (2006). Sodium channel β4 subunit: down-regulation and possible involvement in neuritic degeneration in Huntington's disease transgenic mice. J. Neurochem. *98*, 518–529. https://doi.org/10.1111/j.1471-4159.2006.03893.x.

O'Leary, T., Williams, A.H., Franci, A., and Marder, E. (2014). Cell types, network homeostasis, and pathological compensation from a biologically plausible ion channel expression model. Neuron *82*, 809–821. https://doi.org/10.1016/j.neuron.2014.04.002.

Padovan-Neto, F.E., Sammut, S., Chakroborty, S., Dec, A.M., Threlfell, S., Campbell, P.W., Mudrakola, V., Harms, J.F., Schmidt, C.J., and West, A.R. (2015). Facilitation of corticostriatal transmission following pharmacological inhibition of striatal phosphodiesterase 10A: role of nitric oxide-soluble guanylyl cyclase-cGMP signaling pathways. J. Neurosci. *35*, 5781–5791. https://doi.org/10.1523/JNEUROSCI.1238-14.2015.

Parikh, J., Kozloski, J., and Gurev, V. (2020). Integration of AI and Mechanistic Modeling in Generative Adversarial Networks for Stochastic Inverse Problems (ArXiv).

Planert, H., Berger, T.K., and Silberberg, G. (2013). Membrane properties of striatal direct and indirect pathway neurons in mouse and rat slices and their modulation by dopamine. PLoS One *8*, e57054. https://doi.org/10.1371/journal.pone.0057054.

Ponzi, A., Barton, S.J., Bunner, K.D., Rangel-Barajas, C., Zhang, E.S., Miller, B.R., Rebec, G.V., and Kozloski, J. (2020). Striatal network modeling in Huntington's disease. PLoS Comput.Biol. *16*, e1007648. https://doi.org/10.1371/journal.pcbi.1007648.

Price, K.V. (2013). Differential evolution. Intell.Syst. Ref. Lib. https://doi.org/10.1007/978-3-642-30504-7_8.

Prinz, A.A., Bucher, D., and Marder, E. (2004). Similar network activity from disparate circuit parameters. Nat. Neurosci. *7*, 1345–1352. https://doi.org/10.1038/nn1352.

Ramocki, M.B., and Zoghbi, H.Y. (2008). Failure of neuronal homeostasis results in common neuropsychiatric phenotypes. Nature *455*, 912–918. https://doi.org/10.1038/nature07457.

Raymond, L.A., André, V.M., Cepeda, C., Gladding, C.M., Milnerwood, A.J., and Levine, M.S. (2011). Pathophysiology of Huntington's disease: time-dependent alterations in synaptic and receptor func. Neuroscience *198*, 252–273. https://doi.org/10.1016/j.neuroscience.2011.08.052.

Rodrigues, F.B., and Wild, E.J. (2017). Clinical trials corner: September 2017. J. Huntington's Dis. *6*, 255–263. https://doi.org/10.3233/JHD-170262.

Rogawski, M.A., and Löscher, W. (2004). The neurobiology of antiepileptic drugs for the treatment of nonepileptic conditions. Nat. Med. *10*, 685–692. https://doi.org/10.1038/nm1074.

Ross, C.A., Pantelyat, A., Kogan, J., and Brandt, J. (2014). Determinants of functional disability in Huntington's disease: role of cognitive and motor dysfunction. Mov. Disord. *29*, 1351–1358. https://doi.org/10.1002/mds.26012.

Roukoz, H., and Saliba, W. (2007). Dofetilide: a new class III antiarrhythmic agent. Expert Rev. Cardiovasc. Ther. *5*, 9–19. https://doi.org/10.1586/14779072.5.1.9.

Rumbell, T., and Kozloski, J. (2019). Dimensions of control for subthreshold oscillations and spontaneous firing in dopamine neurons. PLoS Comput.Biol. *15*, e1007375. https://doi.org/10.1371/journal.pcbi.1007375.

Rumbell, T.H., Draguljić, D., Yadav, A., Hof, P.R., Luebke, J.I., and Weaver, C.M. (2016). Automated evolutionary optimization of ion channel conductances and kinetics in models of young and aged rhesus monkey pyramidal neurons. J. Comput. Neurosci. *41*, 65–90. https://doi.org/10.1007/s10827-016-0605-9.

Sarkar, A.X., and Sobie, E.A. (2010). Regression analysis for constraining free parameters in electrophysiological models of cardiac cells.

PLoS Comput. Biol. *6*, e1000914. https://doi.org/10.1371/journal.pcbi.1000914.

Sarkar, A.X., Christini, D.J., and Sobie, E.A. (2012). Exploiting mathematical models to illuminate electrophysiological variability between individuals. J.Physiol. *590*, 2555–2567. https://doi.org/10.1113/jphysiol.2011.223313.

Scala, F., Kobak, D., Bernabucci, M., Bernaerts, Y., Cadwell, C.R., Castro, J.R., Hartmanis, L., Jiang, X., Laturnus, S.R., Miranda, E., et al. (2020). Phenotypic variation within and across transcriptomic cell types in mouse motor cortex. bioRxiv. https://doi.org/10.1101/2020.02.03.929158.

Sebastianutto, I., Cenci, M.A., and Fieblinger, T. (2017). Alterations of striatal indirect pathway neurons precede motor deficits in two mouse models of Huntington's disease. Neurobiol. Dis. *105*, 117–131. https://doi.org/10.1016/j.nbd.2017.05.011.

Sheng, M., Tsaur, M.L., Nung Jan, Y., and Yeh Jan, L. (1992). Subcellular segregation of two A-type K+ channel proteins in rat central neurons. Neuron *9*, 271–284. https://doi.org/10.1016/0896-6273(92)90166-B.

Surmeier, D.J., Bargas, J., and Kitai, S.T. (1988). Voltage-clamp analysis of a transient potassium current in rat neostriatal neurons. Brain Res. *473*, 187–192. https://doi.org/10.1016/0006-8993(88)90334-4.

Talevi, A. (2015). Multi-target pharmacology: possibilities and limitations of the "skeleton key approach" from a medicinal chemist perspective. Front. Pharmacol. *6*, 205. https://doi.org/10.3389/fphar.2015.00205.

Tong, X., Ao, Y., Faas, G.C., Nwaobi, S.E., Xu, J., Haustein, M.D., Anderson, M.A., Mody, I., Olsen, M.L., Sofroniew, M.V., and Khakh, B.S. (2014). Astrocyte Kir4.1 ion channel deficits contribute to neuronal dysfunction in Huntington's disease model mice. Nat. Neurosci. *17*, 694–703. https://doi.org/10.1038/nn.3691.

Virlogeux, A., Moutaux, E., Christaller, W., Genoux, A., Bruyère, J., Fino, E., Charlot, B., Cazorla, M., and Saudou, F. (2018). Reconstituting corticostriatal network on-a-chip reveals the contribution of the presynaptic compartment to Huntington's disease. Cell Rep. *22*, 110–122. https://doi.org/10.1016/j.celrep.2017.12.013.

Wehling, M. (2009). Assessing the translatability of drug projects: what needs to be scored to predict success? Nat. Rev. Drug Discov. *8*, 541–546. https://doi.org/10.1038/nrd2898.

West, A.R., and Grace, A.A. (2004). The nitric oxide-guanylyl cyclase signaling pathway modulates membrane activity states and electrophysiological properties of striatal medium spiny neurons recorded in vivo. J. Neurosci. *24*, 1924–1935. https://doi.org/10.1523/JNEUROSCI.4470-03.2004.

Wolf, J.A., Moyer, J.T., Lazarewicz, M.T., Contreras, D., Benoit-Marand, M., O'Donnell, P., and Finkel, L.H. (2005). NMDA/AMPA ratio impacts state transitions and entrainment to oscillations in a computational model of the nucleus accumbens medium spiny projection neuron. J. Neurosci. *25*, 9080–9095. https://doi.org/10.1523/JNEUROSCI.2220-05.2005.

Zhao, B., Zhu, J., Dai, D., Xing, J., He, J., Fu, Z., Zhang, L., Li, Z., and Wang, W. (2016). Differential dopaminergic regulation of inwardly rectifying potassium channel mediated subthreshold dynamics in striatal medium spiny neurons. Neuropharmacology *107*, 396–410. https://doi.org/10.1016/j.neuropharm.2016.03.037.

Zheng, P., and Kozloski, J. (2017). Striatal network models of Huntington's disease dysfunction phenotypes. Front.Comput.Neurosci. *11*, 70. https://doi.org/10.3389/fncom.2017.00070.

STAR★METHODS

KEY RESOURCES TABLE

REAGENT or RESOURCE	SOURCE	IDENTIFIER
Deposited Data		
Data and Code	This Paper	https://github.com/sallam-usc/Study_Data
Software and Algorithms		
IBM Neural Tissue Simulator	Kozloski and Wagner (2011)	Available from IBM by request to the lead author
Python	Python Software Foundation	https://www.python.org
Evolutionary Algorithm	Rumbell and Kozloski (2019)	https://github.com/BlueBrain/BluePyOpt
		https://senselab.med.yale.edu/ModelDB/ShowModel?model=258643

RESOURCE AVAILABILITY

Lead contact

Further information and requests for code and data should be directed to James Kozloski (kozloski@us.ibm.com).

Materials availability

Materials (code and data) are available from the lead author upon request.

Data and code availability

The data and code used to generate key figures is available in the GitHub link provided above. Some models need to use the IBM Neural Tissue Simulator, which is available from IBM by request to the lead author.

METHOD DETAILS

Model and simulations

The MSN model used in this study was published in Octeau et al.(2019), having been derived with modification from a model published previously by a different group (Mahon et al., 2000). The model comprises a single compartment with eight active ionic conductance models and three specific ionic leak current models. The modifications and channel equations are listed and elaborated below.

Neuron model

The model comprised eight conductance parameters, the transient sodium current (g_{Nat}), persistent sodium current (g_{Nap}), the slowly inactivating sodium current (g_{Nas}), the delayed rectifier potassium current (g_{KDR}), the inward rectifying potassium current (g_{KIR}), the persistent potassium current (g_{KRP}), the fast inactivating A-current (g_{KAf}), the slow inactivating A-current (g_{KAs}). The model also included three specific leak currents for potassium, sodium, and chloride, each based on the Goldman-Hodgkin-Katz (GHK) equation:

$$\varphi_s = P_s z_s^2 \frac{V_m F^2}{RT} \frac{[S_i] - [S_o]\exp(-z_s V_m F/RT)}{1 - \exp(-z_s V_m F/RT)}, \quad \text{(Equation 1)}$$

where ϕ_S is the current density flux (amperes per unit area) of ion S, P_s is the permeability of ion S, $[S_i]$ is the intracellular concentration of ion S, $[S]_o$ is the extracellular concentration of ion S, and V_m is the membrane potential. Reversal potentials for each ion species are then calculated once for all currents using the Nernst equation:

$$E_s = \frac{RT}{zF} \ln\left(\frac{S_o}{S_i}\right),$$

where R is the universal gas constant 8.314 $J \cdot K^{-1} \cdot mol^{-1}$, T is the temperature 295 K, z is the valence of the ionic species, and F is the Faraday's constant 96,485 $C \cdot mol^{-1}$. We set external and internal ion

concentrations to those used for the experiments reported here and in main sections. The calculation of MSN membrane potential in our revised model then follows:

$$C\frac{dV}{dt} = -\left[(V-E_{Na})*\overline{g}_{NaT} + (V-E_K)*\overline{g}_{KDR} + (V-E_K)*\overline{g}_{KIR} + (V-E_K)*\overline{g}_{KRP} + (V-E_K)*\overline{g}_{KAf} + (V-E_K)*\overline{g}_{KAs} + (V-E_{Na})*\overline{g}_{NaS} + (V-E_{Na})*\overline{g}_{NaP} + I_{Cl,leak} + I_{Na,leak} + I_{K,leak} + I_{Inj}\right],$$

where V is the membrane potential, each g is the conductance of an ion channel current (noted by subscript). Ion channel currents followed $I = \overline{g}m^k h(V-E)$. The activation m and optional inactivation h gating variables were as reported in Mahon et al. (2000) followed:

$$\frac{dp}{dt} = \alpha_p(1-p) - \beta_p p\,,\ p\in(m,h,n)$$

For channel Nat and KDR, the gating parameters were as follows:

$$\alpha_m = 0.1(V\text{-}28)/\exp((0.1(V\text{-}28)) - 1)\,,\ \beta m = 4.0\exp(V\text{-}53/18),$$

$$\alpha h = 0.07\exp(0.05(V\text{-}51))\,,\ \beta h = 1/(\exp 0.1(V\text{-}21) + 1)$$

$$\alpha_n = 0.01(V\text{-}27)/\exp((0.01(V\text{-}27)) - 1)\,,\ \beta n = 0.125\exp(V\text{-}37/80)$$

The inactivation for currents followed:

$$\tau(V) = \tau_0 \Big/ \left(\exp^{-\left(V-V\tau/k\tau\right)} + \exp^{\left(V-V\tau/k\tau\right)}\right),$$

except for I_{As}, where $\tau_{hAs}(V) = 1790 + 2930\exp(-(V+38.2/28^2))((V+38.2)/28)$, and I_{KRP}, where $\tau_{KRP}(V) = 3*\tau_{hAs}(V)$. I_{leak} for each specific leak for is derived by multiplying current density flux from Equation 1 by the compartment surface area (assumed to be 1 μm^2). I_{Inj} represents injected current.

For numerical integration, we used a time step of 0.01 ms. All datasets were archival at the time they were shared with researchers from IBM, and no new experiments were suggested, designed, or performed based on these analyses.

Software

All simulations were performed using the IBM Neural Tissue Simulator (NTS) on IBM's Cloud. NTS executes simulations based on model descriptions (written in the Model Description Language) and resource allocation scripts (written in the Graph Specification Language). The software is experimental, and readers are therefore encouraged to contact the authors if interested in using the tool. The MSN model specification for running simulations in NTS with the parameter sets used in this study are available upon request. The parameter sets to run the simulations and reproduce the wild-type and Huntington's disease electrophysiological properties are also available upon request.

Parameter search

Features and stimulation protocols included those to extract membrane resistance from voltage traces elicited by a 5pA depolarizing stimulus for a duration of 200ms. Rheobase was determined using a ramp protocol with a delay of 500 ms and current gradually increased from 0 to 1000pA over 1000msec, effectively with a slope of 1pA/ms.

A large proportion of models entered into the depolarization block. Although certain features are calculable, the results are not deemed accurate, and under further depolarization, not sustainable. Hence, additional feature constraints such as interspike interval coefficient of variation (ISI_CV) and firing rates were added. We conducted multiple checks so that the firing rate was also captured within the time window of the last 1000 ms.

To capture firing rate feature values (spikes/s), and in accordance with data from Planert et al. (2013), three separate protocols were used: firing rates at current injection equal to Rheobase, at Rheobase+50pA

(FR50), and at Rheobase+100pA (FR100). In addition, ISI_CV within an interstimulus interval, after hyperpolarizing potential (AHP), action potential height (AP_height), time to first spike, or spike latency when elicited by Rheobase+50pA and Rheobase+100pA were each targeted as features constrained by the optimization algorithm. Two separate runs of optimizations were performed for WT and HD categories.

It was difficult to find PoMs spanning the complete feature ranges uniformly. We stopped the optimization when we achieved >1200 zero error models. The WT and HD firing rates were targeted to a mean value of 6 spikes/s and a target deviation of 4 spikes/s. In this way, the optimization algorithm would accept a model as a 'good' model if it had a firing rate between 2 and 10 spikes/s.

Selection of population of WT models for analysis

The outcome of the evolutionary algorithm is governed by the random seed chosen and the target feature ranges. We performed 5 optimization trials targeting the entire WT phenotype range using a different random seed in each trial. This resulted in populations of good models (i.e., with zero error) that were clustered in two regions of feature space, which we termed modes A and G, shown in feature space in Figure 2G. Two trials converged to sample points from mode A, and three trials converged to sample points from mode G. The samples from modes A and G, while falling within the high-dimensional hypercube defined as the zero error region for the optimization, were only proximal to a subset of the empirical data points. As it appeared our default optimization settings were only likely to generate models from these two modes, we adjusted the bounds of target features for several additional optimization trials to encourage sampling of points closer to individual empirical data points (see Results for details). These 5 additional trials used 5 of the empirical data points in Vm, Rm, and Rh as target means, with target ranges restricted to $\pm$10% of the original target feature ranges. This approach required a slight relaxation of the remaining feature constraints to encourage the algorithm to return models within the missing regions of entire WT feature space by simply allowing models with non-zero error to be included in the final population for each trial. Figure S1, left, shows the error values for each feature across the different optimization trials (Modes A and G using random seeds and original settings, Modes B-F using feature ranges targeting specific empirical data points), and Figure S1, right, shows the total error for each mode. A summed error of 1.0 across all features means that the features were outside the target ranges by a total of half the range across all features. Modes C and D, with the largest errors, were dominated by errors from the AHP feature, indicating that the main problem with these models was that they did not repolarize to our specified membrane potential for MSNs. Note that these errors stem from features for which we do not have empirical data from Beaumont et al. (2016), and instead are based on prior observations from the literature. This approach enabled us to supplement the dataset gathered using multiple random seeds and led to a larger number of additional modes in feature space attempting to fill the remaining feature space with models from additional optimization runs. The resulting distribution of sampled models is compared with the empirical data distribution in Figure S2. The upper left corner of Figure S2 demonstrates that the combined distribution is highly multimodal. Our analysis methods were designed to work with distributions as close to unimodal as possible (see discussion), so we attempted to downsample the combined distribution using the k-nearest neighbors approach, previously applied in Figure 2B (see results). However, the distributions after downsampling (not shown) were still highly multimodal, which led to the decision to apply our methods to PoMs derived from single optimization results, described in STAR Methods and results.

We constructed two separate databases of PoMs representing the WT and HD phenotypes. To construct the PoMs, we used an evolutionary optimization algorithm, described in detail below.

Population modeling

The optimization employed the non-dominated sorting (NS) differential evolution (DE) algorithm (NSDE) (Deb et al., 2002; Price, 2013) previously used to search parameter space of compartmental neuron models in Rumbel et al. (Rumbell et al., 2016; Rumbell and Kozloski, 2019). To run the algorithm, we used a modified version of the BluePyOpt (Van Geit et al., 2016) Python framework for single neuron optimization. Trial and error was used to assess optimization metaparameters such as population size and number of generations. A single optimization of ~500 generations of a population of ~100 models took ~12 hours of computing time on an X86_64 Intel architecture (2 GHz, 64 bit, 56 cores, 128 Gb of RAM). A neuron model error score for each target feature was calculated by extracting feature measures and subtracting them from the exact target values based on empirical measures and dividing the absolute value of this quantity by a deviation variable based on variability of the experimental measures. Dominance ranking according to the NS

algorithm was used as the first criterion for model selection, and total error was used to sort models within dominance ranks.

The optimizations accessed and varied 11 parameters: ionic conductances $\overline{g}_{NaT}$, $\overline{g}_{NaP}$, $\overline{g}_{NaS}$, $\overline{g}_{KDR}$, $\overline{g}_{KRP}$, $\overline{g}_{KIR}$, $\overline{g}_{KAf}$, and $\overline{g}_{KAs}$ adapted from Mahon et al.(2000), and GHK based permeability coefficients $P_{Cl,\ leak}$, $P_{Na,\ leak}$, and $P_{K,\ leak}$. The optimization algorithm (Rumbell and Kozloski, 2019) was configured using a modified version of the BluePyOpt python package (Van Geit et al., 2016) to produce models whose features fell within either the WT or HD feature ranges specified (Table 1). Additionally, we added a penalty to models that enter depolarization block by using the firing rate features (FR50, FR100) within the time window of 1500 to 2500 ms, to filter out models that did not maintain stable firing activity throughout the stimulation protocol. The parameter conductance ranges (minimum and maximum) were constrained identically for both the WT and HD phenotype-targeted optimizations (Table 2).

We performed multiple optimization runs targeting the entire WT empirical range, with different random seeds and several optimization runs targeting specific individuals in empirical feature space, to identify populations that matched every empirical observation (see Results and Supplementary material for full details of this process). Selection of the final PoMs to represent the WT and HD phenotypes for analysis was based on the individual optimization run with results that most closely matched the empirical targets according to the Wasserstein distance metric (described below).

For the final analysis and virtual drug design presented in the main section of this paper, we selected only models that had zero error score (i.e., had feature values within the target ranges (Table 1) for all features), which we therefore considered 'good models'. In addition, we ensured by inspection that every model within the databases of phenotypes exhibited realistic spiking behavior of MSNs by verifying against several stimulation protocols (see Results).

Virtual drug construction

To identify a coherent target modulation to rescue neuronal excitability in the HD PoM (population of models), we designed virtual drugs (i.e., a set of ion channel parameter perturbations of the HD models) using several statistical and machine learning methods:

1. **Single target perturbation method** used the difference between the mean parameter values of transient sodium conductance and fast inactivating A-type potassium conductance of WT and HD PoMs to construct virtual drugs vd_Nat and vd_KAf.
2. **Linear regression method** used the parameter coefficients calculated from regressing the HD PoM's features against model parameters within a system of linear equations that is solved to compute conductance parameter changes predicted by the regression to transform the mean HD feature values into the mean WT feature values and construct the virtual drug vd_LIN.
3. **Support Vector Machine method** determined the classification boundary between the two phenotypes using a support vector machine (SVM) classifier. SVM is a supervised machine learning algorithm that finds data points closest to a boundary that separates datasets and uses them to help define a linear decision boundary (hyperplane) between data categories. The Python sklearn-SVC package was then used to compute the vector that is normal to the hyperplane separating the two PoMs in parameter space. This vector was then used to effect desired phenotype changes from the HD to the WT PoM and to construct the virtual drug vd_SVM.
4. **n-dimensional histogram method** is a heuristic that took the differences between parameters of each of M members of the WT PoM and parameters of each of N members of the HD PoM's phenotype to construct M × N difference vectors. Difference vectors were binned in the vector space, according to the size of the differences in each parameter. The mode of this multidimensional histogram was then used to effect desired phenotype changes from the HD to the WT PoM and to construct the virtual drug vd_HIST.
5. **Difference of means method** applied the difference between the parameter value means from **Single target perturbation method** to all 11 model parameters to compose a difference vector used to effect desired phenotype changes from the HD to the WT PoM and to construct the virtual drug vd_DIFF.

For each virtual drug, treated HD PoM's parameter vectors were modulated uniformly by adding the vectors obtained for each of the above virtual drug construction methods and are termed HD+*virtual drug*.

Virtual drug validation on different WT population of models

We applied the difference of means method to attempt the rescue of the HD PoM using the WT Mode B PoM and WT Mode G PoM (shown in Figure S3) in the place of the WT PoM used to calculate the vd_DIFF virtual drug. Figure S5 shows the result of applying the vd_DIFF virtual drug at 4 intermediate doses, comparable with the results shown in Figure 6. The ED3 metric is reduced by 99% (Mode B) and 76% (Mode F), and Wasserstein distance metrics are reduced by 40–80%, indicating good recovery of the HD population toward different WT phenotypes. These results suggest that the difference of means method is a reliable method to identify candidate virtual drug profiles that work well in simulation. However, each region of parameter space occupied by WT models provides a slightly different ionic conductance modulation profile, which suggests that candidate virtual drugs should be viewed as a distribution of possible ionic conductance modulators. Selection among these candidates then becomes an additional consideration for a user of these methods.

QUANTIFICATION AND STATISTICAL ANALYSIS

Scoring metrics

We used the following metrics to quantitatively compare the performance of each of the above virtual drugs' effects in rescuing the neuronal excitability of the HD PoM's features:

1. **Euclidean Distance 3D** measures the distance between centroids of two populations of data using three membrane properties: V_m, R_m and Rheobase.
2. **Wasserstein Distance 3D** measures the distance between two probability distributions within the same three-dimensional space of membrane properties. Note this metric is also known as the Earth Mover's Distance. We used this metric to quantify how well the virtual drug minimized the distance between the distributions for two phenotypes.
3. **Total Score** measures the mean of normalized Euclidean Distance 3D and Jensen–Shannon Distance metrics. We used this score to quantify the efficacy of different virtual drugs for recovering the WT PoM from the HD PoM.
4. **Wasserstein Distance 7D** measures the distance between the probability distributions of the WT and HD population data phenotypes derived from seven of the membrane properties listed in Table 1 (excluding FR100 and TFS100, defined below).
5. **Models Retained** counts the number of models within the HD PoM that satisfied the feature constraints of WT ranges listed in Table 1 in order to adhere to the realistic spiking behavior of MSNs after virtual drug perturbations. Models that do not follow the spiking behavior as highlighted in Figures 2C and 2D are models whose features fall outside the pre-defined set of feature range objectives of the evolutionary algorithm or those models where automated feature extraction fails.

Sample size selection

To ensure a fair comparison of Wasserstein distance metric values in the 3-dimensional feature space between empirical data and simulated data, we performed a comparison of Wasserstein distance calculations with different sample sizes. There were 11 samples available in the empirical data, so we performed random sampling from the larger population of simulated models at different samples sizes to check variability in the calculated metric scores. We found only a small change in standard deviation across even very low sample sizes, as shown in Figure S4, for all virtual drug populations. Therefore, we used a sample size of 11 for calculating Wasserstein distance between the WT Mode A and virtual drug PoMs in Figures 7C and 7D, and reported the standard deviations to make a fair comparison with PDE10i.

Other visualization and statistical methods

For analysis of the resulting HD+*virtual drug* PoM, we employed the following:

1. **Convex hull method** used the Python scipy.spatial convex hull package to calculate the hull vertices and edges bounding the 11 data points from each category of WT, HD and HD+PDE10i obtained

from Beaumont et al. (Beaumont et al., 2016), by means of the quick hull algorithm (http://www.qhull.org). This hull is illustrated in Figure 1 for the three categories WT, HD and HD+PDE10i.

2. **K-nearest neighbor search** applies a method for finding a predefined number of points closest in distance to the new point based on standard Euclidean distance. We set nearest neighbors to 2 in order to derive at least two 'matched models' for every real empirical data point in Figure 2A. We used the same approach to identify multiple PoMs closest to empirical observations as shown in Figure 2G.
3. **Statistical methods** to calculate p-values between the empirical and matched models were calculated using the Python scipy.stats package's Kolmogorov-Smirnov (K-S) statistic applied to two samples.